Check for updates

AstroSat detection of Lyman continuum emission from a $z = 1.42$ galaxy

Kanak Saha [1]✉, Shyam N. Tandon[1], Charlotte Simmonds [2], Anne Verhamme[2], Abhishek Paswan[1], Daniel Schaerer [2], Michael Rutkowski [3], Anshuman Borgohain [4], Bruce Elmegreen[5], Akio K. Inoue [6,7], Francoise Combes [8], Debra Elmegreen[9] and Mieke Paalvast[10]

One of the outstanding problems of current observational cosmology is to understand the nature of sources that produced the bulk of the ionizing radiation after the Cosmic Dark Age. Direct detection of these reionization sources[1] is practically infeasible at high redshift (z) due to the steep decline of intergalactic medium transmission[2,3]. However, a number of low-z analogues emitting Lyman continuum at 900 Å restframe are now detected at $z < 0.4$ (refs. [4–8]) and there are also detections in the range $2.5 < z < 3.5$ (refs. [9–14]). Here we report the detection of Lyman continuum emission with a high escape fraction (>20%) from a low-mass clumpy galaxy at $z = 1.42$, in the middle of the redshift range where no detection has been made before and near the peak of the cosmic star-formation history[15]. The observation was made in the Hubble Extreme Deep Field[16] by the wide-field Ultraviolet Imaging Telescope[17] onboard AstroSat[18]. This detection of extreme ultraviolet radiation from a distant galaxy at a restframe wavelength of 600 Å opens up a new window to constrain the shape of the ionization spectrum. Further observations with AstroSat should substantially increase the sample of Lyman-continuum-leaking galaxies at cosmic noon.

Low-mass, compact, actively star-forming emission-line galaxies with high equivalent widths are thought to be promising candidates for sources of escaping Lyman continuum ($\lambda < 912$ Å, hereafter LyC) photons[6,19]. The galaxy AUDFs01 (right ascension, 53.1444 deg; declination, −27.7911 deg) at redshift $z = 1.42$ has been selected from the Hubble Extreme Deep Field[16] and has one of the highest Hα $\lambda 6,563$ Å and [O III] $\lambda 5,007$ Å fluxes, measured by the Hubble Space Telescope (HST) grism G141 under the 3D-HST programme[20]. Both emission lines have high equivalent widths, EW(Hα) = 1,210 Å, EW([O III]) = 1,517 Å, indicating the production of a copious amount of ionizing photons in the galaxy with relatively few old stars. Here we present broad-band imaging observations of this galaxy in the far-ultraviolet (FUV, 1,300−1,750 Å, F154W) and near-ultraviolet (NUV, 2,000−2,800 Å, N242W) filters using the Ultraviolet Imaging Telescope (hereafter, UVIT[17]) onboard AstroSat (see Methods for details about the AstroSat observation, GT05-240, principal investigator Kanak Saha). In the NUV, the galaxy has a magnitude of 25.6 ± 0.1 (±1σ) AB mag with S/N = 10.03. In the FUV band, the source is detected at the same location as in the NUV but with a magnitude of 25.84 ± 0.34 AB mag and S/N = 3.2. In either

case, the magnitudes are aperture and foreground dust corrected. The detected source has a background-subtracted flux 6.7σ above the local background in the FUV band (Methods). The detection of the galaxy in AstroSat FUV and NUV along with HST UV/optical/infrared (IR) is presented in Fig. 1. The Lyman break of the galaxy AUDFs01 is redshifted to an observed wavelength $\lambda_{lim} = 2{,}188.8$ Å (LyC limit for this galaxy) and the FUV filter probes the galaxy in the restframe wavelength range 537−723 Å. This detection of extreme ultraviolet (EUV, $\lambda \approx 600$ Å restframe) photons from a distant galaxy, near the peak of the cosmic star-formation history[15], by AstroSat opens up a window to probing star-forming galaxies with EUV photons. This range of wavelength is where models are least constrained, so our observation puts new constraints on the shape of the ionizing spectrum of stellar populations.

This LyC-leaking galaxy is unique due to its redshift; no LyC escape has been detected in the redshift range $0.4 < z < 2.5$. This galaxy is also unique due to being a distant leaking galaxy with a clumpy morphology. Note that the ionizing radiation ($\lambda \leq 912$ Å) from sources at $z < 2.7$ would fall at an observed wavelength $\lambda < 3{,}374$ Å and would be blocked by the upper atmosphere for ground-based observation. Although the HST Cosmic Origins Spectrograph could have detected sources at this redshift range, the redshift gap ($0.4 < z < 2.5$) remained barren until now. The FUV imaging by AstroSat with a wide field of view may substantially increase the number of LyC-emitting galaxies in this previously undetected redshift range, as the FUV band can exclusively probe LyC emission from galaxies with $z > 0.97$.

We have identified all the objects around AUDFs01 observed by the HST and marked their redshifts from the publicly available 3D-HST survey[20] and the Multi Unit Spectroscopic Explorer (MUSE) Deep Field Survey[21]. We found no other object detected within a circle of diameter 3.2" centred on AUDFs01; all three objects (two with spectroscopic and one with photometric redshift) detected immediately outside this circle are at higher redshift than this galaxy. There is no obvious source of contamination to explain the FUV detection other than coming from the clumpy galaxy AUDFs01. We discuss possible contamination further in Methods.

As marked in Fig. 1, the galaxy has three bright clumps (C1, C2 and C3) and a fainter one (C4)—all appear to be connected by a 12σ surface brightness contour. They are connected in redshift too. In Extended Data Fig. 1, we show the HST grism G141

[1]Inter-University Centre for Astronomy and Astrophysics, Ganeshkhind, India. [2]Observatoire de Genéve, Universitéde Genéve, Versoix, Switzerland. [3]Department of Physics and Astronomy, Minnesota State University-Mankato, Mankato, MN, USA. [4]Department of Physics, Tezpur University, Napaam, India. [5]IBM Research Division, T. J. Watson Research Center, Yorktown Heights, NY, USA. [6]Department of Physics, School of Advanced Science and Engineering, Waseda University, Tokyo, Japan. [7]Waseda Research Institute for Science and Engineering, Waseda University, Tokyo, Japan. [8]Observatoire de Paris, LERMA, College de France, CNRS, PSL University, Sorbonne University, UPMC, Paris, France. [9]Department of Physics and Astronomy, Vassar College, Poughkeepsie, NY, USA. [10]Leiden Observatory, Leiden University, Leiden, The Netherlands. ✉e-mail: kanak@iucaa.in
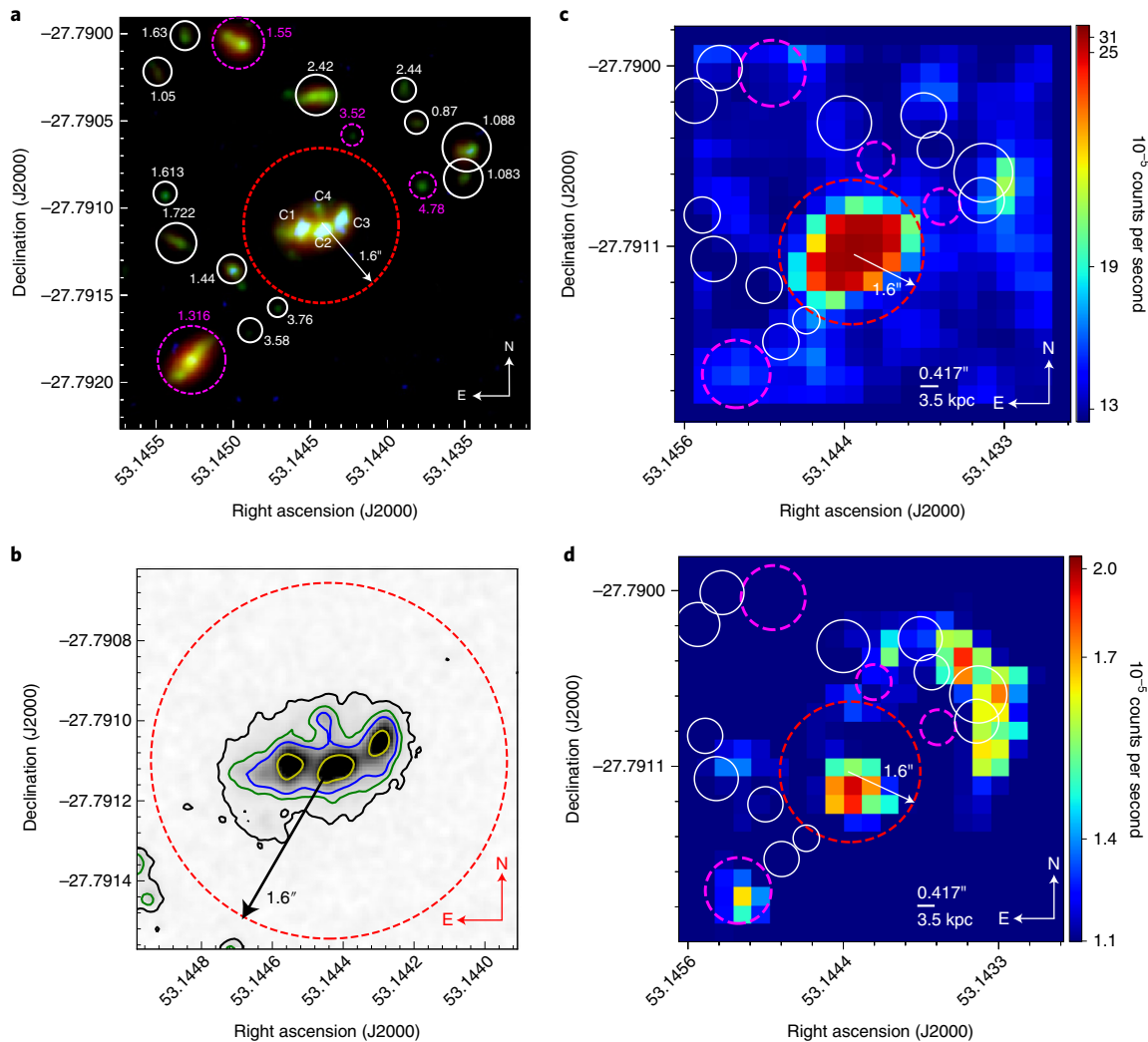
Fig. 1 | Detection of the source in the AstroSat. a, HST colour composite (F275 + F606W + F160W bands) of AUDFs01 in the Hubble Extreme Deep Field. All 14 objects around the galaxy are marked by coloured circles: magenta, spec-z; white, photo-z. **b**, Contour image of the galaxy in F606W band. The outermost contour is at the 3σ (27.25 mag arcsec^{-2}) level and the next level is drawn at the 12σ level, encompassing all the clumps, C1, C2, C3 and C4. The contours in blue and yellow are at the 24σ and 96σ level, respectively. **c,d**, AstroSat observation of AUDFs01 in the NUV (**c**) and FUV (**d**) bands. Both images are smoothed with a Gaussian kernel with a radius of 3 pixels. The brightest pixel within 1.6″ of the FUV image has 4.43×10^{-5} counts per second. The arc-like feature in the FUV image is due to the blending of several sources, some with low redshift, corresponding to non-ionizing restframe FUV emission. In the bottom left corner, the S/N of the FUV emission from the $z = 1.316$ galaxy is too low to claim a positive LyC detection. The right ascension and declination are in degrees in all four panels.

image of AUDFs01 and its full spectrum. The redshift of the galaxy is derived using the Hα line. To derive the redshift of each clump and the spatial origin of the emission lines, we have constructed an emission-line mapping (Methods) of the galaxy (Fig. 2). With that, we have extracted spectra for region 1 (covers C1 + C2), region 2 (C3) and region 3 (C4), marked in Extended Data Fig. 1, and estimate the redshift of each clump using the Hα line (Fig. 2). The Hα emission ($>5\sigma$) from C1, C2 and C3 are consistent with redshift $z = 1.42$. Only when the clumps C1, C2 and C3 were masked, we could extract Hα emission from clump C4. The fitting of the extracted spectrum (Fig. 2c) shows that C4 is at $z = 1.415$. Furthermore, we have also derived the photometric redshift of the clumps by modelling their multiwavelength spectral energy distribution (SED) constructed from the HST observations from F275W to F160W (a total of 11 passbands for each clump) using EAZY[22]. The redshift of each clump is found to be $z \approx 1.42$, consistent with the location of the Balmer break as well as our estimate from the Hα

emission (Fig. 3), establishing the fact that all four clumps are at the same redshift and integral parts of AUDFs01.

Following the N2 method[23], we estimate the oxygen abundance in the galaxy to be $12 + \log[\text{O/H}] = 7.99$, indicating a metal-poor galaxy with metallicity $Z \approx 0.004$. From the emission-line measurements, we obtain O32 = [O III] $\lambda 5,007$/[O II] $3,727 = 9.63$ and R23 = ([O III] $\lambda 5,007, 4,959 +$ [O II] $3,727$])/Hβ $= 10.05$, where [O II] $3,727$ is the sum of the [O II] doublet resolved by MUSE[24]—these values are comparable to those found in the local LyC leakers[6,25].

The high equivalent widths of the emission lines indicate that AUDFs01 is composed of mostly a young population with an ample abundance of hot O-type stars producing energetic ionizing photons. In fact, with EW(Hβ) = 128 Å, EW([Hβ]) + EW([O III]) = 1, 645 Å (680 Å restframe) is comparable to some of the high-z LyC sources[12,26]. Using the Hα line flux, we obtain the star formation rate SFR ≈ 23–$40\,M_\odot$ yr^{-1} for the full galaxy, depending on the adopted attenuation correction and neglecting LyC photon escape[27].
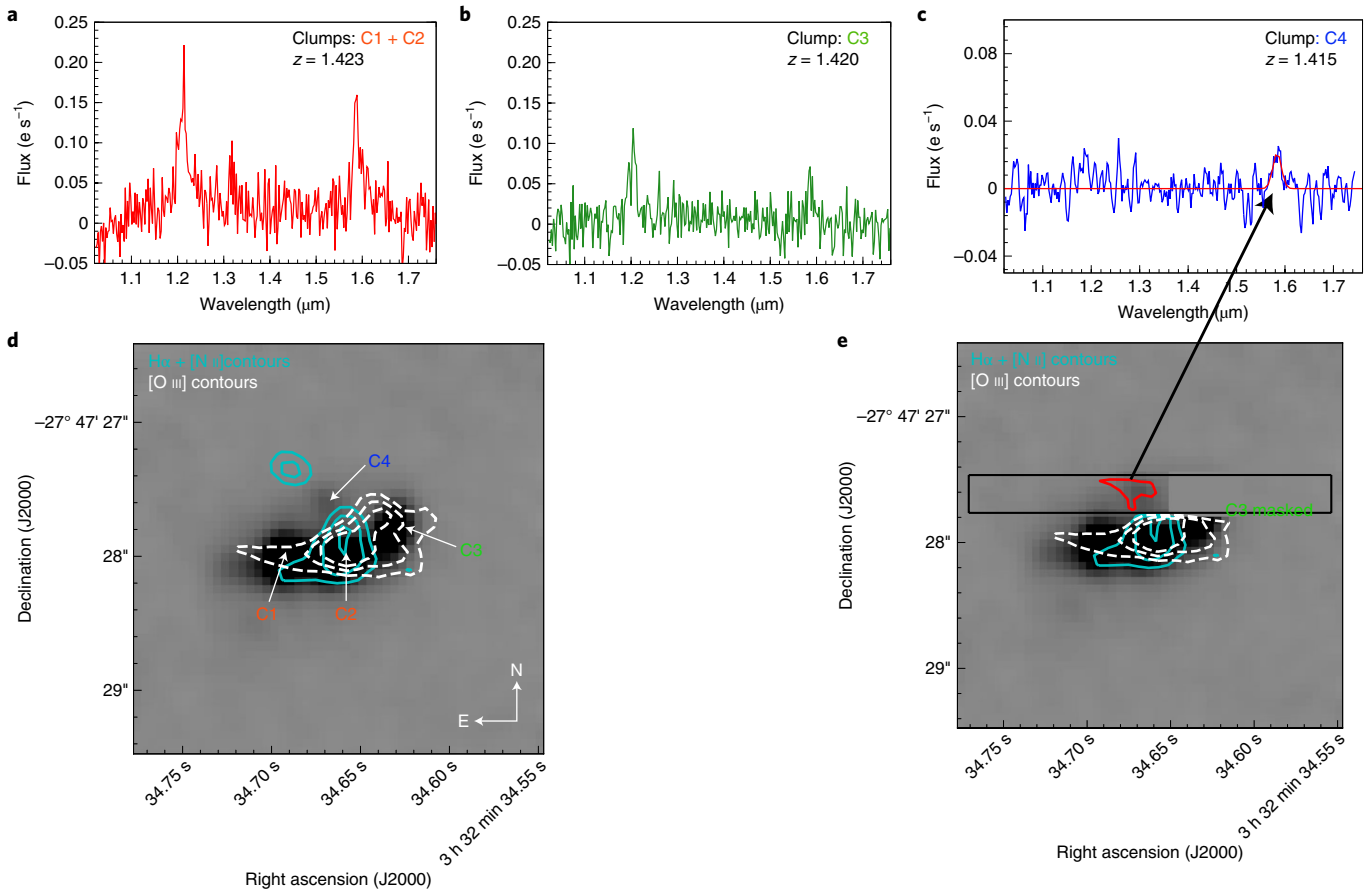
Fig. 2 | Emission-line mapping and clumps. a–c, One-dimensional spectra extracted from C1 + C2 (**a**), C3 (**b**) and C4 (**c**) clump regions (Extended Data Fig. 1). Their redshifts are determined by fitting the Hα line. **d**, Hα and [O III] contours are overplotted on an F160W image at 10σ (inner most), 7σ and 5σ (outer) levels. **e**, The C4 region (red) from which the one-dimensional spectrum is extracted; the detected Hα line flux is >2σ. The source above clump C1 is detected in Hα at $z = 1.433$ but not detected in any other wavelength probed here.

We estimate an age of ~4−6 Myr for the H II regions in the galaxy using the Hβ and Hα equivalent widths and the Starburst99[28] model. Based on the [N II] Baldwin, Phillips and Terlevich (BPT)[29] diagram (Extended Data Fig. 2) and 7 Ms Chandra X-ray observations[30], it is inferred that the galaxy does not host an active galactic nucleus (AGN) (Methods).

The stellar mass and stellar population age of the galaxy are derived by modelling the multiwavelength broad-band SED from the FUV to IR (1,300−45,000 Å) for the whole galaxy (Fig. 3) using both the PCIGALE[31] and the BPASS models[32]. The best-fit PCIGALE model (Fig. 3) with metallicity $Z = 0.004$ yields a continuum colour excess $E(B − V) = 0.15$, and has a total stellar mass of $1.45 \times 10^9 M_\odot$, including a young stellar component of $1.5 \times 10^8 M_\odot$. The age of the main stellar population is ~100 Myr, while the late-burst age is 2 Myr. The integrated SFR is ~55 $M_\odot$ yr^{-1}. To better model the AstroSat FUV flux, we have run a series of BPASS models (Methods) with varying column density, opacity of the intergalactic medium (IGM) along with the photoionization code Cloudy[33]. We found that a low column density $N_H = 10^{17}$ cm^{-2} and younger stellar population of 4−6 Myr are preferred to explain the restframe FUV flux of this source. The best-fit clump SED models (Fig. 3) show that the clump masses are similar to each other, for example: C1, $1.66 \times 10^8 M_\odot$; C2, $2.95 \times 10^8 M_\odot$; C3, $2.31 \times 10^8 M_\odot$; except for C4, $7.30 \times 10^6 M_\odot$. The clump masses of C1, C2 and C3 are relatively higher than those found in local galaxies. However, the clump-to-galaxy mass ratio for AUDFs01 is ~0.47, consistent with known clump-to-galaxy mass ratios at this redshift in the Great Observatories Origins Deep Survey (GOODS) region[34].

The low-mass and clumpy morphology of the galaxy favour the escape of the LyC radiation from the galaxy as they offer more surface area for leaking. However, observing such LyC radiation depends on the properties of the interstellar medium in the galaxy as well as the IGM between us and the galaxy. When LyC radiation escapes a galaxy, it is redshifted on its way to the observer, as long as it is not absorbed by an intervening H I cloud. The probability of encountering such a cloud depends on the redshift of the emitting source. The IGM absorption is higher at higher redshift ($z > 3$), while at lower redshift ($z < 0.4$), the transmission is always high. At intermediate redshift, the IGM transmission distribution shows characteristic bimodality; at the redshift of our object ($z = 1.42$), the median IGM transmission is 0.74 and the median optical depth $\tau_{IGM} = 0.29$ (refs. [3,35]) in the AstroSat F154W band, which probes solely LyC radiation. We consider the IGM bimodality in our calculation of escape fraction of LyC photons, denoted as f_{esc}.

We use the observed Hα flux corrected for attenuation from UV slope (Extended Data Fig. 5) to estimate the number of LyC photons that are absorbed in the galaxy to be $N_{LyC}^{non-esc} = (2.12 \pm 0.22) \times 10^{54}$ s^{-1}. The restframe luminosity of the galaxy in F154W is $1.68 \pm 0.45 \times 10^{43}$ erg s^{-1} corresponding to an escaping LyC photon rate of $N_{LyC}^{emit} = 0.54 \pm 0.14 \times 10^{54}$ s^{-1} at the mean wavelength of ~600 Å. This results in an absolute escape fraction of $f_{esc} = 0.2$ for $E(B − V) = 0.13$ and $\tau_{IGM} = 0$ (see equation (9)). We obtain a relatively higher escape fraction $f_{esc} = 0.5$ from the PCIGALE best-fit SED model, which incorporates CLOUDY modelling and where the free parameter f_{esc} was varied from 0 to
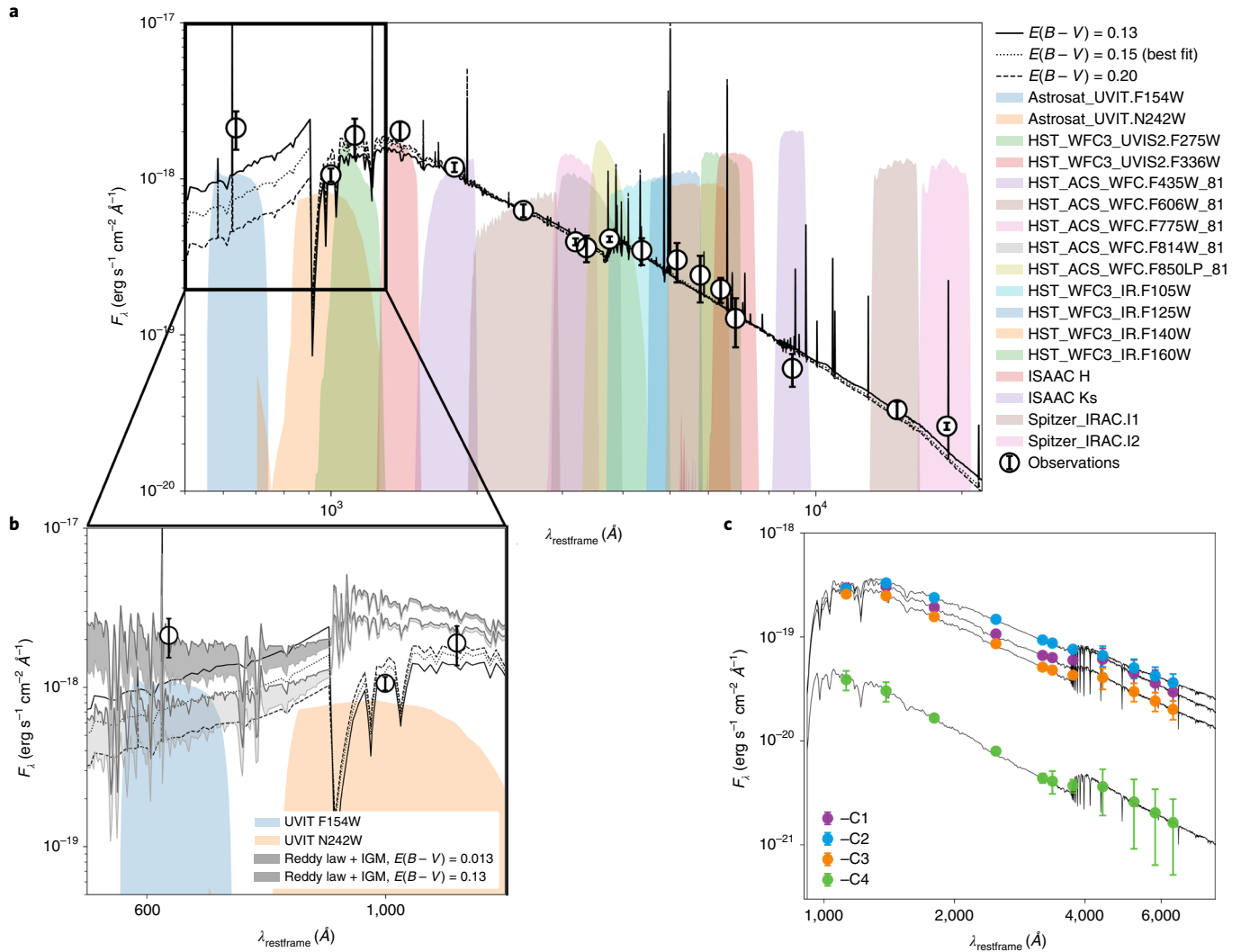
Fig. 3 | Modelling of SED. a, Stellar + nebular emission models based on BC03 stellar populations are fitted to the observed SED using PCIGALE with varying parameters (Extended Data Fig. 6). The error bars denote 1σ uncertainties in all panels. The coloured shaded regions are the bandpasses of various filters (see legend) used in this analysis. The best-fit model (dotted line) is the one with $E(B-V) = 0.15$ and $Z = 0.004$. **b**, The BPASS modelling of the AstroSat UV fluxes with the Reddy extinction law. The grey shaded region reflects the IGM distribution with transmission from 0.4 to 1.0. None of these models alone can reproduce the photometry of AUDFs01 perfectly from restframe 600 to 18,595 Å. **c**, Clump SED modelling using EAZY[22], primarily to determine their photometric redshift. Plotted lines are the best-fit SED models.

0.8 along with a set of other parameters (Extended Data Fig. 6). We also derive the escape fraction by comparing the observed LyC flux with the one expected from stellar population models with the age of 4.5 Myr estimated from EW(Hβ) and EW(Hα) using the frequently used relation[4,6,28]. Considering $E(B-V) = 0.13$ and assuming a transparent IGM, we obtain $f_{esc} \approx 0.31$; while for the median IGM transmission, $f_{esc} \approx 0.42$. Our estimates of f_{esc} are broadly consistent with each other. Based on our calculations, the $z = 1.4$ clumpy galaxy is emitting at least ~20% of ionizing photons towards the IGM.

In Fig. 4a, we compile known sources that are spectroscopically confirmed LyC emitters. In the relatively low-redshift universe ($z < 0.4$), 11 LyC emitters have been identified among the population of Green Pea galaxies, using HST-COS[6,8,36,37]; and in the more distant Universe ($z > 3.0$), 15 individual detections were reported among the population of Lyman break galaxies, using the Keck Low Resolution Imaging Spectometer[13]. All flux ratios are given in F_λ. A few more LyC emitters were reported recently in the literature, such as the strongly lensed Sunburst Arc at $z \approx 2.4$ (ref. [38]),

or Ion3 and Ion4 at $z \approx 3$ and $z \approx 4$, respectively[12], with comparable $F_{LyC}/F_{1,500}$. Our source, observed in the FUV and NUV with AstroSat/UVIT[18,39], is unique from two points of view. First, the EUV range of the spectrum of a star-forming galaxy, around 600 Å restframe; and second, AstroSat is opening up a new redshift range for searches of LyC emitters at $z \approx 1-2$, where the IGM is still fairly transparent (Fig. 4b). At the redshift of our source, more than 80% of the lines of sight have a transmission above 80% at 900 Å restframe; and at 600 Å restframe, almost 50% of the lines of sight have a transmission better than 80%, illustrating the potential of AstroSat to detect efficiently a great number of LyC emitters over $z \approx 1-2$ and so far unexplored restframe LyC wavelength ranges. Detecting LyC emitters at lower z is important because the fainter sources can be seen at closer distances and there are, in general, many more smaller galaxies than the larger ones. Perhaps, the smaller ones dominated the reionization. Future samples of LyC emitters that are likely to be discovered in the AstroSat UV Deep Field (AUDF) in the FUV and NUV bands, have the potential to unveil the nature of the sources responsible for the production of
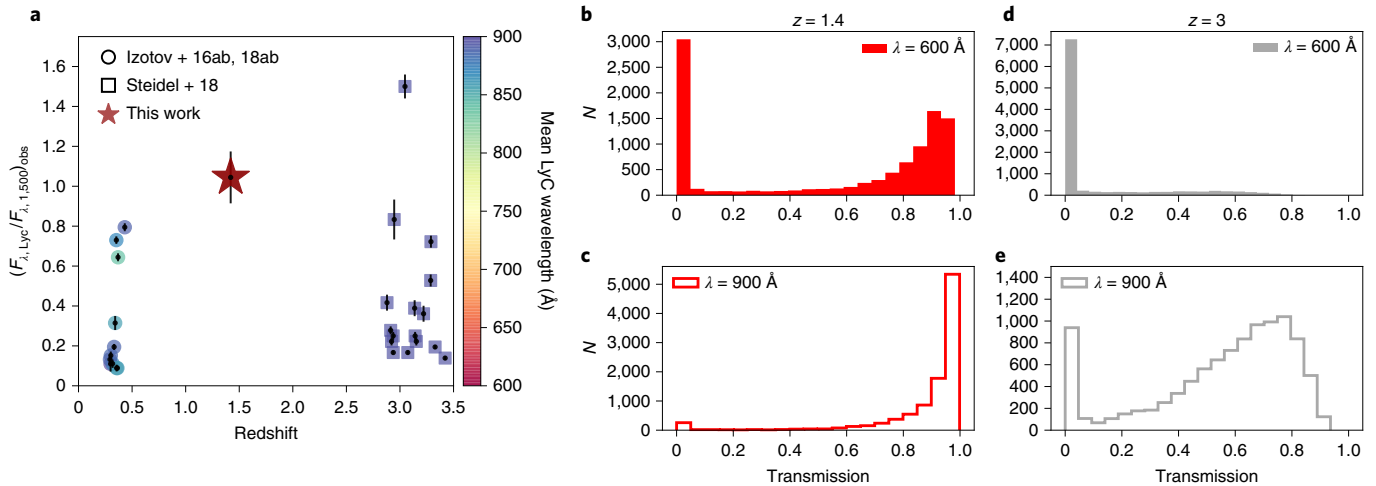
Fig. 4 | Comparison of AUDFs01 with other confirmed LyC detection and IGM distribution. a, Objects with spectroscopically confirmed LyC detection (so far) are compared with our source found in the redshift desert. The FUV flux detected by AstroSat-UVIT for AUDFs01 at $z \approx 1.42$ corresponds to high-energy EUV photons at a restframe wavelength of $537 - 723$ Å. The error bars represent 1σ uncertainties on the flux measurements. Izotov + 16ab, 18ab refer to refs. [6,8,36,37] and Steidel + 18 refers to ref. [13]. **b–d**, Distribution of IGM transmissions along 10,000 lines of sight computed using Monte Carlo simulations[3], for 600 Å (**b,d**) and 900 Å (**c,e**), and for $z \approx 1.4$ (**b,c**) and $z \approx 3$ (**d,e**).

this EUV radiation and improve our understanding of the sources that have led to cosmic reionization.

Methods

A flat Λ cold dark matter (where Λ is the cosmological constant) cosmology with $H_0 = 70$ km s^{-1} Mpc^{-1}, $\Omega_m = 0.3$ and $\Omega_\Lambda = 0.7$ was adopted throughout the article, where H_0 is the Hubble constant, and Ω_m and Ω_Λ refer to matter and dark energy density, respectively . All magnitudes quoted in the paper are in the AB system.

AstroSat observation and other archival data. The clumpy galaxy AUDFs01 was selected from the Hubble Extreme Deep Field (XDF), having one of the deepest Wide Field Camera 3 (WFC3)/IR images. We first searched the 3D-HST[20] GOODS-South catalogue of 1,517 galaxies with spectroscopic redshift and non-zero, positive Hα, [O III] and Hβ fluxes. The simultaneous presence of these emission lines is possible only for galaxies in the redshift range $1.1 < z < 1.55$, the so-called redshift desert[40,41]. This reduces our sample of 1,517 to 948 galaxies. Of these, only 38 galaxies are in the Hubble XDF (denoted as stars symbol in Extended Data Fig. 2). The clumpy galaxy AUDFs01 is chosen as one having the highest [O III] and Hα fluxes and stellar mass around $\sim 10^9 M_\odot$, indicating a vigorous star-formation activity. The photometry for the full galaxy uses archival HST imaging data in the UV (F275W, F336W), optical (WFC/Advanced Camera for Surveys (ACS): F435W, F606W, F775W, F814W and F850LP) and IR (WFC3: F105W, F125W, F140W and F160W). Also, we use the archival Very Large Telescope/Infrared Spectrometer And Array Camera (VLT/ISAAC) observation in the H and Ks bands and Spitzer/IRAC data in the 3.6 and 4.5 μm bands. Extended Data Fig. 3 shows their postage stamp images from the Galaxy Evolution Explorer (GALEX) FUV to Spitzer 4.5 μm band.

The FUV and NUV imaging data come from AstroSat observations of the GOODS-South field (GT05-240; principal investigator, Kanak Saha). These observations were carried out by UVIT (with a field of view (FOV) of 28′ diameter) onboard AstroSat, which performed simultaneous observation in the F154W and N242W bands during September–October 2016. The observation was carried out for 100 kilosec, which corresponds to ~100 orbits. During each orbit, FUV and NUV observation in photon counting mode were taken every 33 ms, resulting in about 45,000–50,000 frames (in each band) accumulation in a good orbit. The orbit-wise dataset was processed using the official L2 pipeline, in which we removed frames that were affected by the cosmic-ray shower and those frames were excluded in the final science-ready images and the subsequent calculation of photometry. This has resulted in ~15% loss of data to science-ready images. In addition to this, there was data loss due to the mismatch of the time stamp on the VIS (visual) filter and the NUV or FUV filters. The final science-ready image of the AUDF had a total exposure time of $t_{exp} = 63938.5$ s in the FUV and 62341.1 s in the NUV corresponding to ~63 AstroSat orbits.

We perform differential astrometry in two steps: first, we use GALEX deep field data of the GOODS-South region. Followed by this step, we use the HST F606W optical image of the GOODS-South as a reference image and redo the astrometric correction. We use an IDL programme, which takes an input set of matched

x pixel/y pixel (from the UVIT image) and right ascension/declination (from the F606W image) and perform a TANGENT-Plane astrometric plate solution similar to the ccmap task of IRAF. The astrometric accuracy in the NUV is found to be ~0.2″ while for the FUV, the root mean square (RMS) ~0.3″ (note, a pixel ~0.4″). The photometric calibration is performed with a white dwarf star Hz4; the photometric zero-points[17] are 17.78 and 19.81 for F154W and N242W, respectively. Once photometric calibration and astrometric correction are successfully applied, we extract an image of the same size as the Hubble XDF from the UVIT full FOV and run SExtractor[42] on it. We have extracted all sources that have $S/N \geq 3$ using the following relation:

$$S/N = \frac{S \times t_{exp}}{\sqrt{S \times t_{exp} + B \times N_{pix} \times t_{exp}}}, \qquad (1)$$

In the above equation, S denotes the background-subtracted source flux within a given aperture (with N_{pix} as the number of pixels), B is the background within the same aperture and t_{exp} denotes the exposure time in the same passband. In writing the above equation, we have neglected read noise, which is null in the CMOS detector used in UVIT. The dark current is about $10 e^- s^{-1}$ over the full circular FOV (diameter 28′) corresponding to ~7.8×10^{-7} ct s^{-1} pix^{-1}. Note that the dark current in our detector is about ten times smaller than the background as estimated below. The background (B) measured directly from the science-ready image includes this dark current contribution. Once all the sources are detected in the original science image, we mask sources with $S/N \geq 5\sigma$. Then we re-run SExtractor and remove all the sources $\geq 3\sigma$ and produce a masked image again. We use this masked image to create a histogram out of N (roughly a few thousand) random apertures of 1.6" radius placed all over the image, avoiding the source locations. This histogram appears slightly positively skewed. Furthermore, we remove sources $> 2.75\sigma$ and then carried out the same exercise as above. The histogram on this residual image is found to be nearly symmetric, and fitted with a Gaussian distribution. We reach a global sky surface brightness (mean value) of 28.6 mag arcsec^{-2} and 27.8 mag arcsec^{-2} in the FUV and NUV bands, respectively. The 3σ detection limit for point source within 1" radius in the FUV is 27.9 AB mag.

The same procedure has been applied to a smaller cutout ($100'' \times 100''$) around AUDFs01 to estimate the local background appropriate for the galaxy. The local mean from the Gaussian fit is $B = 5.7 \times 10^{-6}$ ct s^{-1} pix^{-1} (or 28.9 mag arcsec^{-2}) and a background RMS, $\sigma_{bkg} = 6.8 \times 10^{-6}$ ct s^{-1} pix^{-1}.

We estimate the source + background flux (F_{SB}) within an aperture of radius 1.6" ($N_{pix} = 46$) for AUDFs01. By considering the astrometric error of ~0.3 , we randomly place 25 such 1.6" apertures about the location of AUDFs01. The mean source + background flux is $<F_{SB}> = (5.71 \pm 0.058) \times 10^{-4}$ ct s^{-1} (the median is 5.74×10^{-4}). From this, we obtain the mean background-subtracted source flux as $S = 3.1 \times 10^{-4}$ ct s^{-1} corresponding to 26.5 AB mag without any aperture correction and foreground dust correction in the FUV band. Throughout this paper, we have used directly measured fluxes and noise from a given aperture to estimate the S/N. The aperture-plus-dust-corrected magnitudes for AUDFs01 in different bands are presented in Extended Data Fig. 7. With the estimated local background and using equation (1), we obtain $S/N = 3.2$ for AUDFs01 in the FUV.

The detected source has a flux 6.7σ ($=S/\sqrt{N_{\mathrm{pix}}}\sigma_{\mathrm{bkg}}$) above the local background in the same F154W band.

Other sources. We have examined all the 38 sources in the HST F606W band as mentioned above. We identify only those objects that are clean, such that there are no other sources (in particular, ones with $z < 0.97$) present within the 1.6" aperture. We found nine sources that satisfy this criterion and of these, two refer to the same source. So we are left with only eight sources. Of these eight sources, only two sources have $S/N \geq 3$ detection in the F154W band of AstroSat. Of these, we picked AUDFs01 with the highest [O III] and Hα fluxes as well as equivalent widths. The other source at $z = 1.29$ (53.176, -27.773) had a lower [O III] flux as well as equivalent width (EW[O III] $= 36.9$ Å). This source, together with all other upper limits, will be described in a forthcoming paper. Note that the galaxy at $z = 1.316$ as shown in Fig. 1a has F154W flux detected at $S/N = 2.5$. When we inspected the F606W image carefully, we found another object within a circle of 1.6" of this galaxy; although the object has a photo-z $z = 3.58$, we restrict ourselves to spectroscopic redshift only for the purpose of clean LyC detection. None of the sources on the northwest corner (forming an arc-like feature) of the F154W image (Fig. 1) has spectroscopic redshift; all of them have photo-z with $z > 0.97$, except one at $z = 0.87$. The FUV emission (for example, centred on sources at $z = 1.083$ and 1.088) is indeed stronger ($\sim 3\sigma$), but all these sources are blended in F154W band due to the large FUV point spread function (PSF), making an arc-like appearance on the smoothed FUV image. The non-leaking source at $z = 0.87$ is a foreground contamination to the rest.

Contamination hypothesis. *An intervening star.* Could the AstroSat FUV flux be due to a 'contamination' from an intervening star, invisible at longer wavelengths? This is extremely unlikely, as it would correspond to the chance alignment of an early type star at megaparsec distances. Indeed, to explain the observed flux $F_{1,500} \approx 2 \times 10^{-18}\,\mathrm{erg\,s^{-1}\,cm^2\,Å^{-1}}$ with an unreddened O4V star (with $T_{\mathrm{eff}} = 43{,}000\,\mathrm{K}$, $\log(L/L_\odot) = 5.7$)[43] would imply a distance of the order of $\sim 50\,\mathrm{Mpc}$. Even for much fainter hot stars with similar temperatures, this would imply unrealistically large distances. If the star was substantially reddened, it would be detected at longer wavelengths and hence be distinguishable as such from the SED and the available spectra.

An interloper galaxy. The possibility of the AstroSat FUV flux being due to a foreground galaxy, invisible at longer wavelengths, is also unlikely. As such a contaminating galaxy would be bright in the FUV, it would be a star-forming galaxy, with nebular recombination lines emitted from H II regions. The Lyman-α emission from a foreground Lyman-α emitter at $0.069 < z < 0.439$ would fall in the AstroSat FUV broad band. Assuming that part of the flux detected by AstroSat would be due to this emission line, we argue that the associated optical nebular lines, Hα and the strong [O III] doublet ($\lambda4{,}959, \lambda5{,}007$ Å), would be detected in the MUSE data[24]. We extract a MUSE spectrum within a round 1.6" aperture, to compare with the AstroSat detection, and examined the spectrum in detail. Neither of the two lines mentioned above are detected in the MUSE spectrum, at any wavelength corresponding to the redshift window where the AstroSat FUV detection would correspond to a foreground Lyman-α emitter. The only emission lines detected in the spectrum are Mg II and [O II] from AUDFs01, at $z \approx 1.42$. The flux density measured by AstroSat in the FUV is FUV $= 2.12 \times 10^{-18}\,\mathrm{erg\,s^{-1}\,cm^{-2}\,A^{-1}}$. Assuming a Lyman-$\alpha$ equivalent width as weak as 2 Å, this translates into a predicted Hα flux $F(\mathrm{H}\alpha) > 2 \times \mathrm{FUV}/8.7 \approx 5 \times 10^{-19}\,\mathrm{erg\,s^{-1}\,cm^{-2}}$. This lower limit is calculated assuming case B and an escape fraction of Lyman-α emission of 100%. All escape fractions from Lyman-alpha Emitters (LAEs) reported in the literature are (much) lower, so the expected line fluxes in the optical are (much) stronger.

Assuming that the detection in AstroSat is only due to the UV continuum of a foreground galaxy, the detected FUV magnitude, 25.84, would correspond to an SFR $\approx 3\,M_\odot\,\mathrm{yr^{-1}}$, translating to an H$\alpha$ line flux of $\sim 3 \times 10^{-17}\,\mathrm{erg\,s^{-1}\,cm^{-2}}$. Given that the 3σ detection threshold for an emission line in the MUSE deep data is $3 \times 10^{-19}\,\mathrm{erg\,s^{-1}\,cm^{-2}}$, we would be able to detect the optical nebular lines associated with an intervening galaxy.

Another line of argument is to estimate the probability of detecting a LAE along the sightline. A cylinder of the Universe with a section of 1.6 and a length corresponding to $0.069 < z < 0.439$ would subtend a volume of $\sim 0.6\,\mathrm{Mpc^3}$. From previous GALEX studies (Fig. 13 in Wold et al.[44]), the number of galaxies with Lyman-α luminosities around $10^{41}\,\mathrm{erg\,s^{-1}}$ is as low as 10^{-3} objects per $\mathrm{Mpc^3}$ (brighter galaxies are even less numerous). So we would need a volume of $1{,}000\,\mathrm{Mpc^3}$ to have one chance alignment.

Comparing with HST/F150LP detection. It is important to compare our results with a previous search[45] for LyC leakers in the redshift range, $1.1 < z < 1.5$ with deep FUV imaging of the HST/XDF field in the ACS/SBC F150LP band. When we examined the F150LP image, we were unable to identify any source at the location of AUDFs01 confirming the previous conclusion[45]. The non-detection of AUDFs01 in the HST data can be understood from the sensitivity differences of the two images at the location of the source.

Although the read noise is 0 e$^-$ in both Solar Blind Channel/Multi Anode Microchannel Array (SBC/MAMA) and UVIT/CMOS, the dark current is higher

in SBC/MAMA[46,47]; it is $\sim 1.2 \times 10^{-5}\,\mathrm{e^-\,s^{-1}\,pix^{-1}}$ (see ACS quick reference guide, cycle 15, 2005 (http://documents.stsci.edu/hst/acs/documents/handbooks/cycle15/c03_intro_acs6.html)). In comparison, we have a dark current of $7.8 \times 10^{-7}\,\mathrm{e^-\,s^{-1}\,pix^{-1}}$. Accounting for the proper pixel scales and using the HST/F150LP weight image, we estimate the total background noise at the location of AUDFs01 and compare that with the UVIT/F154W image. Using the total background noise, we compute the 3σ upper limit as 28.2 (within 0.5" radius), 27.4 (1.0") and 27.2 (1.2") AB mag. The same for the F154W image are 28.7 (0.5"), 27.9 (1.0") and 27.7 (1.2") AB mag. This shows that the background noise is higher in the HST/F150LP image compared with the F154W image. One can also think that UVIT is more sensitive to low-surface-brightness objects because it has a lower spatial resolution and thereby samples more angular area per unit detector element.

Then we estimate the magnitudes of a few brighter sources common between the two images. For example, a source at 53.14472, -27.7854 (in the vicinity of AUDFs01) has 23.7 AB mag (aperture corrected) in F150LP image while it is 23.77 AB mag (aperture corrected) in F154W. Within errors, these are nearly the same. Using this comparison, we compute the expected flux within 1" radius for AUDFs01 in HST/F150LP band. We chose 1" as an intermediate aperture because 0.5" is too small for the UVIT while 1.6" is large for the HST. In the F154W image, the background-subtracted flux for AUDFs01 is $1.16 \times 10^{-4}\,\mathrm{ct\,s^{-1}}$ within 1.0" (2.4 pix) radius. This would produce $0.008\,\mathrm{ct\,s^{-1}}$ within 1.0" in F150LP image. The corresponding magnitude is 27.7 AB mag while the detection limit within 1" is 27.4 AB mag. This is, of course, a simple calculation (for example, assumed wavelength coverage for two filters the same); there could be a number of other reasons that we are not aware of.

There are other differences between the two observations as well: the median exposure time at the location of AUDFs01 is 5,262 s in the F150LP image, while in the F154W image it is 63,938 s. The blueward cut-off for the F154W filter is 135 nm while that for F150LP is 145 nm. We have checked that between 135 and 145 nm, the F154W filter would contain about 12% of the total flux for the best-fit CIGALE SED model of AUDFs01.

Spectral analysis and emission-line mapping. All four clumps (C1, C2, C3 and C4) in AUDFs01 can be identified in the HST optical (F435W, F606W, F775W, F814W, F850Lp), IR (F105W, F125W, F140W and F160W) and UV (F275W, F336W) bands. By analysing the WFC3/F160W imaging data, we find that the centroids of the clumps C1 and C2 are aligned within a pixel while C3 and C4 are well separated. We use the clump centroids and the position angle (PA = 130°) information to perform astrometric solution to the two-dimensional direct image (3D-HST ID 25778) in F160W. The F160W direct image is utilized to create an emission-line mapping of the grism G141 image. We then extract the continuum plus the contamination-subtracted grism spectra for each of four regions marked in Extended Data Fig. 1. Both region 1 and region 2 contain two prominent broad emission lines, [O III] and Hα. We choose the Hα line to determine the spectroscopic redshift for region 1 and region 2, which turn out to be at $z = 1.420$ and 1.423 for region 1 and region 2, respectively. There is no prominent (5σ or above) emission in the grism data from clump C4. But after masking region 1 (C1 and C2) and region 2 (C3), we found clear Hα emission from C4. The Hα emission from C4 is modelled with a Gaussian; the line flux is obtained to be $4.64 \times 10^{-17}\,\mathrm{erg\,s^{-1}\,cm^{-2}}$ and the redshift of C4 is found to be $z = 1.415$. Such masking became possible only after creating an emission-line mapping, which allowed us to relate pixel-to-pixel mapping between the grism and F160W direct image provided by the 3D-HST observation. By fitting the contamination- and continuum-subtracted HST grism G141 spectra with a Gaussian function, we have extracted the emission-line properties of the full galaxy—in particular, the colour excess $E(B-V)$ and oxygen abundance.

Dust attenuation. *UV slope method.* The UV spectral slope β (where $f_\lambda \approx \lambda^\beta$) is a sensitive indicator of the dust attenuation and hence can be used to estimate the continuum colour excess $E(B-V)$. The parameter β can be formally defined[48] as:

$$\beta = -\frac{m(\lambda_1) - m(\lambda_2)}{2.5\log(\lambda_1/\lambda_2)} - 2 \tag{2}$$

where $m(\lambda_1)$ and $m(\lambda_2)$ are the AB magnitudes of the galaxy at rest-wavelength λ_1 and λ_2, respectively, where according to Calzetti et al.[49], the rest-wavelength $\lambda \in [1{,}268 - 2{,}580]$ Å. Using the above relation, we find $\beta = -2.0 \pm 0.26$ for AUDFs01. Then following the $E(B-V)$ and β relationship[50] appropriate for high-z galaxies, the continuum colour excess is given by

$$E(B-V) = \frac{1}{4.684}[\beta + 2.616] = 0.13 \pm 0.05 \tag{3}$$

It has been shown that star-forming galaxies on the main-sequence relation in the redshift range $1 < z < 2.5$, follow a flatter relation between attenuation and UV slope than Meurer relation[51]. Although AUDFs01 lies above the main-sequence relation, we estimate the colour excess assuming Calzetti reddening curve and the following relation

$$E(B - V) = \frac{1}{k(1,600\,\text{Å})}[1.26\beta + 3.90] \approx 0.14 \pm 0.03 \qquad (4)$$

Our best-fit CIGALE SED model (discussed in 'Multiwavelength SED modelling') yields $E(B - V) = 0.15$ in close agreement with that derived from the UV spectral slope β.

Balmer decrement method. The grism G141 is ideal to capture two of the prominent emission lines such as [O III] 5,007 and Hα for star-forming galaxies in the redshift range $1.1 < z < 1.5$. In this work, we utilize the emission-line data from grism G141 observed under the 3D-HST programme[20]. The nebular colour excess can be estimated using the method of Balmer decrement[52] assuming a case B recombination, temperature $T = 10^4$ K and electron density $n_e = 100$ cm^{-3} as:

$$E(B - V) = 1.97\log\left[\frac{(\text{H}\alpha/\text{H}\beta)_{\text{obs}}}{2.86}\right], \qquad (5)$$

where Hα and Hβ are the observed line fluxes. In the grism G141, the Hα and [N II] lines are blended. We use a prescription based on equivalent width[53] to extract the [N II] 6,583 Å line intensity from the blended Hα line. Further, we have extracted the N II 6,548 Å line flux by applying the atomic transition probabilities[54] such that the ratio of [N II] 6,583/[N II] 6,548 = 2.93. Using the measured fluxes in equation (5), we obtain $E_{\text{nebular}}(B - V) = 0.48 \pm 0.40$. Note the large uncertainty in the determination of nebular colour excess comes from the poor S/N of the Hβ measurement in the grism G141. In fact, this has been one of the major uncertainties in estimating the dust extinction using Balmer decrement at this redshift range. Moving ahead, we use the Calzetti relation to estimate the continuum colour excess $E_{\text{star}}(B - V) = 0.44 E_{\text{nebular}}(B - V) = 0.21$. Since continuum colour excess estimated using the UV β-slope method and PCIGALE SED fitting are in close match with each other, we prefer to use the value from the UV β slope, that is, $E(B - V) = 0.13$ throughout this paper unless mentioned otherwise.

The [O II] line flux is extracted from the MUSE archival data[24]. It is extinction corrected and slit loss is null in the image slicing mechanism used in the MUSE IFU[21]. All the emission-line fluxes from the grism and MUSE are corrected for the foreground galactic extinction[55] of $A_V = 0.019$ mag and further corrected for the internal extinction with a continuum colour excess $E(B - V) = 0.13$ derived from the UV β slope. Finally, the line luminosities are derived using a luminosity distance of $D_L = 10,194.6$ Mpc and these are presented in Extended Data Fig. 5.

Oxygen abundance. The oxygen abundance in the galaxy is estimated following the N2 method[23]:

$$12 + \log[\text{O/H}] = 8.90 + 0.57 \times \text{N2} = 7.99, \qquad (6)$$

where N2 $= \log[\text{N II}] 6,583/\text{H}\alpha = -1.59$. In terms of solar metallicity, [O/H] $\approx 1/5$ solar, indicating a metal-poor galaxy with $Z = 0.0042$. In this calculation, we used [N II] 6,583 and Hα fluxes derived following the method of equivalent width[53].

We have also estimated oxygen abundance using line fluxes from 3D-HST catalogue fluxes. In all cases, the N2 method gives $Z \approx 0.004$.

In addition, we have also used the O3N2 method[23] following the relation

$$12 + \log[\text{O/H}] = 8.73 - 0.32 \times \text{O3N2} = 7.92,$$

where O3N2 $= \log\frac{[\text{O III}]/\text{H}\beta}{[\text{N II}]/\text{H}\alpha} = 2.52$. In terms of solar metallicity, [O/H] $\approx 1/6$ solar, indicating again a metal-poor galaxy with $Z = 0.0034$. As the O3N2 relation is valid only for O3N2 ≤ 1.9, we restrict to the N2 method in this work.

We have used the emission lines to construct the BPT[29] and mass-excitation diagram[56] for the Galaxy (Extended Data Fig. 2). It is inferred that the Galaxy does not host an obvious AGN; it belongs to the star-forming galaxies (SFG) in the BPT. The galaxy is not detected in the 2 Ms or the 7 Ms Chandra source catalogue[30], confirming the non-AGN nature. The same has been confirmed when we compare AUDFs01 with the z-COSMOS SFGs at $z = 0.84$ with [O III]/Hβ and [O II]/Hβ ratios[57]. When searched in the Atacama Large Millimeter/submillimeter Array (ALMA) deep fields, within an RMS of 35 μJy, there is no detection in the 1.3 mm continuum[58,59], indicating less of a molecular gas content in parts of the galaxy. From this, we obtain an upper limit of $M_{\text{gas}} < 10^9 M_\odot$, in close agreement with our estimate ($M_{\text{gas}} = 2.2 \times 10^8 M_\odot$) from SED fitting.

Multiwavelength SED modelling. *CIGALE modelling.* We have constructed a multiwavelength SED from the FUV to IR (1,300–45,000 Å) for the full galaxy (Fig. 3). For the F154W and N242W bands, we have used a fixed circular aperture of radius 0.9" and applied the method of growth curve correction to estimate the total flux of the galaxy. The same procedure was followed to estimate fluxes in VLT/ ISAAC H and Ks bands, and Spitzer/IRAC 3.6 and 4.5 μm bands; in that we have obtained growth curve correction factor in each of these bands. In the case of the HST also, we have used a fixed aperture of 0.9" to calculate the flux and applied the aperture correction—this has been followed throughout all bands of the HST used in the final SED construction. In each case, we examine the region around the object carefully by eye to ensure that there is no contamination from other sources. The error on the measured fluxes is estimated using the available archival

weightmaps. Our measurement of fluxes are given in Extended Data Fig. 7 and these values are in good agreement with 3D-HST measurements[20]; for example, our F775W flux corresponds to 24.16 ± 0.05 AB mag whereas the 3D-HST catalogue value is 24.19 ± 0.03 AB mag.

The physical properties of AUDFs01 have been derived by fitting the stellar population model with nebular lines using PCIGALE[31] as well as using binary stellar population BPASS[32]. In the PCIGALE modeling, we use the BC03 stellar population library[60] with exponentially declining star-formation histories and late bursts. We employ a Salpeter initial mass function (IMF)[61] with lower and upper mass cutoffs at 0.1 and 100 $M_\odot$ respectively. The metallicity values used are 0.0004, 0.004, 0.008 and 0.02; note that the metallicity from our emission-line measurements is $Z \approx 0.004$. The colour excess was varied from $E(B - V) = 0.11–0.22$. This range was chosen from our estimates of colour excess derived based on UV spectral slope (0.13) and Balmer decrement (0.21). In the SED modelling, we followed the Calzetti relation $E_{\text{star}}(B - V) = 0.44 E_{\text{nebular}}(B - V)$; although there is a considerable debate ongoing for high-redshift galaxies[62]. We apply the Calzetti extinction law[63] for dust modelling. The dust attenuation curve has a UV bump at 2,175 Å with amplitude ~1/3 of that of the Milky Way bump and the overall power-law slope of the curve is fixed at $n = -\delta + 0.75 = 1.25$, where δ is the slope deviation. This slope is similar to the slope of the Small Magellanic Cloud (SMC) extinction curve, which may be more appropriate for high-redshift SFGs[64]. The slope deviation (δ) closely matches with the relation[64]: $\delta = -0.38 + 0.29 \times (\log M_* - 10)$. Various modules and their parameters used in the SED modelling are given in Extended Data Fig. 6 and their detailed description can be found here[31]. For the CIGALE models that are shown in Fig. 3, we have fixed $Z = 0.004$, IMF to Salpeter, ionization parameter to -3.0; $E(B - V)$ factor to 0.44 and some of the dust parameters as in Extended Data Fig. 6 but we have allowed $E(B - V)$ to vary from 0.11 to 0.22 in steps of 0.01; f_{esc} was varied from 0 to 0.8, in steps of 0.1. The best-fit PCIGALE model is chosen based on the minimum χ^2 value as well as one that closely matches the ratio of EW of the observed lines (for example, Hα, [O III]) from the HST grism G141. The best-fit PCIGALE model yields $E(B - V) = 0.15$ and $f_{\text{esc}} = 0.5$. Since the best-fit continuum colour excess $E(B - V)$ is close to one from the UV β-slope method, we have also obtained a CIGALE model with $E(B - V) = 0.13$ (UV slope) and for the sake of completeness with $E(B - V) = 0.2$ (Balmer decrement) (Fig. 3). In both cases, the modelling was done exactly in the same way as for the best-fit but with $E(B - V)$ fixed. For $E(B - V) = 0.13$ case, the model yields $f_{\text{esc}} = 0.45$. The best-fit CIGALE model shows an emission-line He I 635 Å falling in the observed FUV band. We have estimated the total flux by integrating the best-fit model over the F154W band with and without the 635 Å line. We found the line flux contributes to 2% of the total flux without the line and conclude that this alone could not have boosted the observed FUV flux.

BPASS modelling. As an independent method, we used simple stellar population models to estimate the age and metallicity range in which our observations could be reproduced. These assume that all stars are born at the same time and distributed according to their IMF. In particular, we used BPASS[32] models to create a grid (Extended Data Fig. 6) that allowed us to explore several different spectral shapes. In addition, we used these spectra to simulate a photoionized region using the software Cloudy[33]. Most parameters were maintained fixed, varying only the stopping condition of the code, in our case determined by column density. To obtain results in which some ionizing radiation escapes, it was necessary to probe low-column-density values (10^{16}, 10^{17} and 10^{18} cm^{-2}). Furthermore, we explored all of the models available in Starburst99[28]. The results were consistent with the ones found using BPASS spectra, indicating a low metallicity ($Z/Z_\odot \approx 0.004$) and young stellar age ($<5 \times 10^6$ yr). As a test, we computed the ratios $f_{\lambda,600}/f_{\lambda,1500}$ and $f_{\lambda,900}/f_{\lambda,1500}$ for all the analysed models and confirmed the possibility of obtaining the observed ratios using any of the models in the mentioned metallicity and age ranges. It is important to note that in this analysis, we used the intrinsic stellar spectra provided by the models to avoid making as many assumptions as possible.

In Fig. 3, we show the chosen BPASS spectra after being run through the photoionization code Cloudy[33]. The chosen parameters are $Z = 0.004$, age $= 5 \times 10^6$ yr, ionization parameter $U = -1.5$ and $\log N_H = 17$ cm^{-2}. This choice was made based on the closeness to the AstroSat observations, which happen to be the same main parameters as those found by a CIGALE fitting. To obtain a more realistic result, we applied some dust extinction and IGM attenuation. For the first one, we used the extinction law by Reddy et al.[65]. This law is only valid down to 950 Å; however, as there is no reliable extinction law below this limit, we decided to extrapolate to lower wavelengths as an approximation. For the second one, we used Monte Carlo simulation[3,35] to find the appropriate range of IGM attenuation. IGM transmission, being extremely stochastic, depends heavily on the line of sight observed. Our analysis of the transmission values at 600 Å and intermediate redshift reveals a bimodal behaviour (Fig. 4b). The transmission distribution allows only values either close to 0 or close to 1 at lower wavelengths, high or low, with 50% of the lines of sight having a transmission above 80%. Since ionizing photons were detected, it is reasonable to assume that the transmission is high along our particular line of sight.

Clump SED modelling. We have used 11 passbands of the HST UV/optical/IR to construct SED for each clump, with wavelength ranging from 2,750 to 16,000 Å,

containing the 4,000 Å break. For this purpose, we have used all HST images with 0.06" resolution. The flux of each clump has been extracted by placing a square box with a fixed size of 0.3" around each centroid of C1, C2, C3 and C4 in the F606W image. Then we have made measurements away from the clumps, by placing the box at seven different locations including intra-clump as well as the outskirts of the galaxy. We take the mean of these measurements and subtract it from C1, C2 and C3 to determine their fluxes. For C4, we made three such measurements— left, right and top of the C4 centroid. The mean of these three measurements is subtracted from C4, to determine the C4 flux. This process is repeated identically for all 11 passbands. These fluxes are corrected for the galactic extinction[55] and the magnitudes of the clumps are presented in Extended Data Fig. 7 along with the full galaxy. We then derive the photometric redshift of each clump by modelling their SED using EAZY[22]. In this fitting, we take into account of the IGM absorption[2] and let the redshift vary from $z = 0.1$ to 6.0. The photometric redshifts obtained are: C1 at $z = 1.39$; C2 at $z = 1.7$; C3 at $z = 1.42$; and C4 at $z = 1.40$. Our photometric redshift estimates are in close agreement with those derived from the grism G141 spectrum extracted for each clump. We then perform CIGALE modelling to derive physical parameters of the clumps using the best-fit SED parameters of the full galaxy, for example, we use $E(B - V) = 0.15$ and $Z = 0.004$. We found the masses of the clumps C1, C2 and C3 to be similar to each other while C4 is ~100 times lower than the rest.

Ionizing photon production and escape fraction. The amount of leaking ionizing radiation is estimated from the observed number of LyC photons (N_{LyC}^{obs}) and that are intrinsically produced in the system (N_{LyC}^{int}). Assuming case B recombination, temperature $T = 10^4$ K and electron density $n_e = 100$ cm^{-3}, we estimate the number of LyC photons that are capable of ionizing hydrogen atoms using the extinction-corrected Hα luminosity[54,66]:

$$N_{LyC}^{non-esc} = \frac{\alpha_B(H^0, T_e)}{\alpha_{H\beta}^{eff}(H^0, T_e)} \frac{\lambda_{H\beta}/\lambda_{H\alpha}}{j_{H\alpha}/j_{H\beta}} \frac{L_{H\alpha}}{h\nu_{H\alpha}} = 7.28 \times 10^{11} L_{H\alpha} \quad (7)$$

where $L_{H\alpha}$ is the luminosity of the Hα emission line, $j_{H\alpha}/j_{H\beta}$ denotes the intrinsic ratio of Hα and Hβ line intensity, α_B and $\alpha_{H\beta}^{eff}$ are the case B recombination rate and Hβ emissivity[54] respectively. Other symbols have the usual meaning. The extinction-corrected Hα luminosity is estimated to be $(29.2 \pm 3.0) \times 10^{41}$ erg s^{-1} corresponding to $N_{LyC}^{non-esc} = (2.12 \pm 0.22) \times 10^{54}$ s^{-1}. A similar relation could be obtained for the Hβ luminosity.

We estimate the rate of LyC photons that escape the galaxy directly from the FUV flux measured at the F154W filter by AstroSat, which probes $537-723$ Å restframe photons for this galaxy. The restframe luminosity of the galaxy in F154W is $(1.68 \pm 0.45) \times 10^{43}$ erg s^{-1} corresponding to about $N_{LyC}^{emit} = 0.54 \pm 0.14 \times 10^{54}$ LyC photons per second (a lower limit, since we exclude the number of ionizing photons that are in the bluer part of the N242W filter). Considering a transparent IGM ($\tau_{IGM} = 0$) and the median value of $\tau_{IGM} = 0.29$ along our line of sight, at this redshift, the escape fraction would be given by

$$f_{esc} = \frac{N_{LyC}^{emit} e^{\tau_{IGM}}}{N_{LyC}^{emit} e^{\tau_{IGM}} + N_{LyC}^{non-esc}} = 0.20 \pm 0.027 \quad (8)$$

$$= 0.25 \pm 0.029 \quad (9)$$

To correct for IGM attenuation, we divide f_{esc} from equation (8) by the IGM transmission along the line of sight. But this peculiar attenuation is not known, only the statistics of the IGM attenuation are known (see right panel in Extended Data Fig. 4). The shape of the distribution of escape fractions corresponding to the distribution of non-zero IGM transmission is shown in the left panel of Extended Data Fig. 4. Since we detect AUDFs01 in the FUV filter, the IGM transmission along our line of sight is non-zero, and we keep only the non-zero transmission of the distribution. The probability of occurrence of each escape fraction bin is normalized to the total number of non-zero transmissions. The distribution of escape fraction peaks around 0.2 and most of the sightlines (90%) have $0.20 < f_{esc} < 0.31$ (Extended Data Fig. 4a).

In the PCIGALE modelling[31], nebular emission is modelled using nebular templates[67] that are generated using Cloudy[33] given a range of metallicity and ionization parameters. In that, the line luminosities are rescaled by the ionizing photon luminosity. The two primary factors that affect the ionization rate of the surrounding gas are f_{esc}, a fraction of the LyC photons that simply escape, and f_{dust}, a fraction of LyC photons that are being absorbed or scattered by the dust. In the PCIGALE modelling, both are free parameters and f_{esc} was varied from 0 to 0.8 (Extended Data Fig. 6). While doing the SED modelling, we have always aimed at reducing the number of parameters to be constrained. The relevant parameter range that was varied to obtain models presented in Fig. 3 is mentioned in 'Multiwavelength SED modelling'. The best-fit PCIGALE model yields a value of $E(B - V) = 0.15$, $f_{dust} = 0.15$ and $f_{esc} = 0.5$.

In a third method, the LyC escape fraction is derived by comparing the observed LyC flux to the intrinsic one expected from stellar population models using the following relation[4,6]:

$$f_{esc} = \frac{(f_{600}/f_{1,500})^{obs}}{(f_{600}/f_{1,500})^{int}} e^{\tau_{IGM}} 10^{-0.4 A_\lambda(1,500)} \quad (10)$$

where $A_\lambda = k_\lambda E(B - V)$; $f_{1,500}$ and f_{600} are the flux densities at restframe wavelength. In writing the above equation, it has been assumed that the dust affects only the non-ionizing radiation in the Galaxy. A similar assumption has been implemented in a number of other published articles that compute the absolute escape fraction[13]. Dust attenuation in the ionizing spectrum of galaxies remains a complex problem as it would depend on several factors of dust properties that are hard to constrain in observation. For example, the dust fraction itself could be low in highly star-forming, metal-poor galaxies[68] or there could be transparent holes in the interstellar medium[62] through which ionizing radiation would escape without substantial attenuation. Note that the original equation[4,6] uses f_{900} as a proxy for the ionizing flux. This paper uses the f_{600} flux (defined as the average flux density at 600 Å), for the same (as in equation (10)). The observed ratio of the flux densities at these wavelengths is obtained as $(f_{600}/f_{1,500})^{obs} = 1.045$ and from the BPASS SED modelling, we have $(f_{600}/f_{1,500})^{int} = 1.17$ for the age of the population, 4.5 Myr. The attenuation is obtained following Reddy extinction curve[62] at $\lambda = 1,500$ Å and is given by $A_\lambda(1,500) = k_\lambda(1,500) E(B - V) = 8.73 \times E(B - V)$. Then using $E(B - V) = 0.13$, we obtain $f_{esc} = 0.31$ (for $\tau_{IGM} = 0$) and $f_{esc} = 0.42$ (for $\tau_{IGM} = 0.29$).

The precise value is strongly dependent on the assumed intrinsic value of f_{600}. The whole distribution of escape fractions for our best-guess stellar model is shown in Extended Data Fig. 4, right panel. It peaks around 0.34; and 90% of the sightlines have $0.31 < f_{esc} < 0.42$. The right panel also shows f_{esc} distribution for other BPASS models with varying ages. We have derived escape fractions from three different methods and get consistent results, so the true escape fraction of restframe 600 Å LyC radiation from AUDFs01 is certainly >20%, given the actual knowledge of stellar templates in the EUV.

Data availability

The HST data are available at https://3dhst.research.yale.edu/Data.php and https://archive.stsci.edu/prepds/hlf. The VLT/ISAAC H- and Ks-band data are available at ESO Science Archive Facility (http://archive.eso.org/scienceportal/home). The Spitzer GOODS-South data used in the analysis are available from https://irsa.ipac.caltech.edu/data/SPITZER/GOODS. The SDSS data are available at the Sloan Digital Sky Survey (https://www.sdss.org). The MUSE spectroscopic data for AUDFs01 is available The other data that support the plots within this paper and other findings of this study are available from the corresponding author upon reasonable request.

Code availability

We have used standard data reduction tools in Python, IDL, IRAF and the publicly available code SExtractor (https://www.astromatic.net/software/sextractor) for this study. For SED fitting and analysis, we have used publicly available code CIGALE (https://cigale.lam.fr), EASY (http://www.astro.yale.edu/eazy/) and BPASS (https://bpass.auckland.ac.nz/2.html). The photoionization code CLOUDY used in this paper is in the public domain (https://trac.nublado.org/). The pipeline used to process the level 1 AstroSat/UVIT data can be downloaded from http://astrosat-ssc.iucaa.in.

References

1. Stiavelli, M., Fall, S. M. & Panagia, N. Observable properties of cosmological reionization sources. *Astrophys. J.* **600**, 508–519 (2004).
2. Madau, P. Radiative transfer in a clumpy universe: the colors of high-redshift galaxies. *Astrophys. J.* **441**, 18–27 (1995).
3. Inoue, A. K., Shimizu, I., Iwata, I. & Tanaka, M. An updated analytic model for attenuation by the intergalactic medium. *Mon. Not. R. Astron. Soc.* **442**, 1805–1820 (2014).
4. Leitet, E., Bergvall, N., Hayes, M., Linné, S. & Zackrisson, E. Escape of Lyman continuum radiation from local galaxies. Detection of leakage from the young starburst Tol 1247-232. *Astron. Astrophys.* **553**, A106 (2013).
5. Borthakur, S., Heckman, T. M., Leitherer, C. & Overzier, R. A. A local clue to the reionization of the Universe. *Science* **346**, 216–219 (2014).
6. Izotov, Y. I. et al. Eight per cent leakage of Lyman continuum photons from a compact, star-forming dwarf galaxy. *Nature* **529**, 178–180 (2016).
7. Leitherer, C., Hernandez, S., Lee, J. C. & Oey, M. S. Direct detection of Lyman continuum escape from local starburst galaxies with the cosmic origins spectrograph. *Astrophys. J.* **823**, 64 (2016).
8. Izotov, Y. I. et al. J1154+2443: a low-redshift compact star-forming galaxy with a 46 per cent leakage of Lyman continuum photons. *Mon. Not. R. Astron. Soc.* **474**, 4514–4527 (2018).
9. Shapley, A. E. et al. Q1549-C25: a clean source of Lyman-continuum emission at $z = 3.15$. *Astrophys. J.* **826**, L24 (2016).
10. Vanzella, E. et al. Hubble imaging of the ionizing radiation from a star-forming galaxy at $Z = 3.2$ with $f_{esc} > 50\%$. *Astrophys. J.* **825**, 41 (2016).

11. Bian, F., Fan, X., McGreer, I., Cai, Z. & Jiang, L. High Lyman continuum escape fraction in a lensed young compact dwarf galaxy at $z = 2.5$. *Astrophys. J.* **837**, L12 (2017).

12. Vanzella, E. et al. Direct Lyman continuum and Ly α escape observed at redshift 4. *Mon. Not. R. Astron. Soc.* **476**, L15–L19 (2018).

13. Steidel, C. C. et al. The Keck Lyman Continuum Spectroscopic Survey (KLCS): the emergent ionizing spectrum of galaxies at $z \sim 3$. *Astrophys. J.* **869**, 123 (2018).

14. Fletcher, T. J. et al. The Lyman continuum escape survey: ionizing radiation from [O III]-strong sources at a redshift of 3.1. *Astrophys. J.* **878**, 87 (2019).

15. Madau, P. & Dickinson, M. Cosmic star-formation history. *Ann. Rev. Astron. Astrophys.* **52**, 415–486 (2014).

16. Illingworth, G. D. et al. The HST Extreme Deep Field (XDF): combining all ACS and WFC3/IR data on the HUDF region into the deepest field ever. *Astrophys. J. Suppl.* **209**, 6 (2013).

17. Tandon, S. N. et al. In-orbit performance of UVIT and first results. *J. Astron. Astrophys.* **38**, 28 (2017).

18. Singh, K. P. et al. ASTROSAT mission. *Proc. SPIE* **9144**, 91441S (2014).

19. Naidu, R. P., Forrest, B., Oesch, P. A., Tran, K.-V. H. & Holden, B. P. A low Lyman continuum escape fraction of <10 per cent for extreme [O III] emitters in an overdensity at $z \sim 3.5$. *Mon. Not. R. Astron. Soc.* **478**, 791–799 (2018).

20. Momcheva, I. G. et al. The 3D-HST survey: Hubble Space Telescope WFC3/G141 grism spectra, redshifts, and emission line measurements for ~100,000 galaxies. *Astrophys. J. Suppl.* **225**, 27 (2016).

21. Bacon, R. et al. The MUSE Hubble Ultra Deep field survey. I. Survey description, data reduction, and source detection. *Astron. Astrophys.* **608**, A1 (2017).

22. Brammer, G. B., van Dokkum, P. G. & Coppi, P. EAZY: A fast, public photometric redshift code. *Astrophys. J.* **686**, 1503–1513 (2008).

23. Pettini, M. & Pagel, B. E. J. [O III]/[N II] as an abundance indicator at high redshift. *Mon. Not. R. Astron. Soc.* **348**, L59–L63 (2004).

24. Inami, H. et al. The MUSE Hubble Ultra Deep Field Survey. II. Spectroscopic redshifts and comparisons to color selections of high-redshift galaxies. *Astron. Astrophys.* **608**, A2 (2017).

25. Cardamone, C. et al. Galaxy Zoo Green Peas: discovery of a class of compact extremely star-forming galaxies. *Mon. Not. R. Astron. Soc.* **339**, 1191–1205 (2009).

26. de Barros, S. et al. An extreme [O III] emitter at $z = 3.2$: a low metallicity Lyman continuum source. *Astron. Astrophys.* **585**, A51 (2016).

27. Kennicutt, R. C. Jr. Star formation in galaxies along the Hubble sequence. *Ann. Rev. Astron. Astrophys.* **36**, 189–232 (1998).

28. Leitherer, C. et al. Starburst99: synthesis models for galaxies with active star formation. *Astrophys. J. Suppl.* **123**, 3–40 (1999).

29. Baldwin, J. A., Phillips, M. M. & Terlevich, R. Classification parameters for the emission-line spectra of extragalactic objects. *Publ. Astron. Soc. Pac.* **93**, 5–19 (1981).

30. Luo, B. et al. The Chandra Deep Field-south Survey: 7 Ms source catalogs. *Astrophys. J. Suppl.* **228**, 2 (2017).

31. Boquien, M. et al. CIGALE: a Python code investigating galaxy emission. *Astron. Astrophys.* **622**, A103 (2019).

32. Eldridge, J. J. et al. Binary population and spectral synthesis version 2.1: construction, observational verification, and new results. *Pub. Astron. Soc. Aus.* **34**, e058-61 (2017).

33. Ferland, G. J. et al. The 2013 release of Cloudy. *Rev. Mex. Astron. Astrofis.* **49**, 137–163 (2013).

34. Elmegreen, D. M. et al. Clumpy galaxies in goods and gems: massive analogs of local dwarf irregulars. *Astrophys. J.* **701**, 306–329 (2009).

35. Inoue, A. K. & Iwata, I. A Monte Carlo simulation of the intergalactic absorption and the detectability of the Lyman continuum from distant galaxies. *Mon. Not. R. Astron. Soc.* **387**, 1681–1692 (2008).

36. Izotov, Y. I. et al. Detection of high Lyman continuum leakage from four low-redshift compact star-forming galaxies. *Mon. Not. R. Astron. Soc.* **461**, 3683–3701 (2016).

37. Izotov, Y. I. et al. Low-redshift Lyman continuum leaking galaxies with high [O III]/[O II] ratios. *Mon. Not. R. Astron. Soc.* **478**, 4851–4865 (2018).

38. Rivera-Thorsen, T. E. et al. Gravitational lensing reveals ionizing ultraviolet photons escaping from a distant galaxy. *Science* **366**, 738–741 (2019).

39. Tandon, S. N. et al. In-orbit calibrations of the ultraviolet imaging telescope. *Astron. J.* **154**, 128 (2017).

40. Steidel, C. C. et al. A survey of star-forming galaxies in the $1.4 \lesssim z \lesssim 2.5$ redshift desert: overview. *Astrophys. J.* **604**, 534–550 (2004).

41. Renzini, A. & Daddi, E. Wandering in the redshift desert. *Messenger* **137**, 41–45 (2009).

42. Bertin, E. & Arnouts, S. SExtractor: software for source extraction. *Astron. Astrophys. Suppl.* **117**, 393–404 (1996).

43. Martins, F., Schaerer, D. & Hillier, D. J. A new calibration of stellar parameters of galactic O stars. *Astron. Astrophys.* **436**, 1049–1065 (2005).

44. Wold, I. G. B. et al. Faint flux-limited Ly emitter sample at ~ 0.3. *Astrophys. J.* **848**, 108 (2017).

45. Siana, B. et al. New constraints on the Lyman continuum escape fraction at z ~ 1.3. *Astrophys. J.* **668**, 62–73 (2007).

46. Teplitz, H. et al. Far-ultraviolet imaging of the Hubble Deep Field-north: star formation in normal galaxies at $z < 1$. *Astron. J.* **132**, 853–865 (2006).

47. Timothy, J. G. Review of multianode microchannel array detector systems. *J. Astron. Telesc. Instrum. Syst.* **2**, 030901 (2016).

48. Nordon, R. et al. The far-infrared, UV, and molecular gas relation in galaxies up to $z = 2.5$. *Astrophys. J.* **762**, 125 (2013).

49. Calzetti, D., Kinney, A. L. & Storchi-Bergmann, T. Dust extinction of the stellar continua in starburst galaxies: The ultraviolet and optical extinction law. *Astrophys. J.* **429**, 582–601 (1994).

50. Reddy, N. et al. The HDUV Survey: a revised assessment of the relationship between UV slope and dust attenuation for high-redshift galaxies. *Astrophys. J.* **853**, 56 (2018).

51. Meurer, G. R., Heckman, T. M. & Calzetti, D. Dust absorption and the ultraviolet luminosity density at $z \sim 3$ as calibrated by local starburst galaxies. *Astrophys. J.* **521**, 64–80 (1999).

52. Osterbrock, D. E. & Ferland, G. J. *Astrophysics of Gaseous Nebulae and Active Galactic Nuclei* 2nd edn (University Science Books, 2006).

53. Sobral, D. et al. Star formation at $z = 1.47$ from HiZELS: an Hα+[O II] double-blind study. *Mon. Not. R. Astron. Soc.* **420**, 1926–1945 (2012).

54. Osterbrock, D. E. *Astrophysics of Gaseous Nebulae and Active Galactic Nuclei* (University Science Books, 1989).

55. Schlegel, D. J., Finkbeiner, D. P. & Davis, M. Maps of dust infrared emission for use in estimation of reddening and cosmic microwave background radiation foregrounds. *Astrophys. J.* **500**, 525–553 (1998).

56. Juneau, Stéphanie et al. Active galactic nuclei emission line diagnostics and the mass–metallicity relation up to redshift $z \sim 2$: the impact of selection effects and evolution. *Astrophys. J.* **788**, 88 (2014).

57. Sobral, D. et al. HiZELS: a high-redshift survey of Hα emitters—II. The nature of star-forming galaxies at $z = 0.84$. *Mon. Not. R. Astron. Soc.* **398**, 75–90 (2009).

58. Dunlop, J. S. et al. A deep ALMA image of the Hubble Ultra Deep Field. *Mon. Not. R. Astron. Soc.* **466**, 861–883 (2017).

59. Franco, M. et al. GOODS-ALMA: 1.1 mm galaxy survey. I. Source catalog and optically dark galaxies. *Astron. Astrophys.* **620**, A152 (2018).

60. Bruzual, G. & Charlot, S. Stellar population synthesis at the resolution of 2003. *Mon. Not. R. Astron. Soc.* **344**, 1000–1028 (2003).

61. Salpeter, E. E. The luminosity function and stellar evolution. *Astrophys. J.* **121**, 161 (1955).

62. Reddy, N. A., Steidel, C. C., Pettini, M., Bogosavljević, M. & Shapley, A. E. The connection between reddening, gas covering fraction, and the escape of ionizing radiation at high redshift. *Astrophys. J.* **828**, 108 (2016).

63. Calzetti, D. et al. The dust content and opacity of actively star-forming galaxies. *Astrophys. J.* **533**, 682–695 (2000).

64. Salim, S., Boquien, M. & Lee, J. C. Dust attenuation curves in the local universe: demographics and new laws for star-forming galaxies and high-redshift analogs. *Astrophys. J.* **859**, 11 (2018).

65. Reddy, N. A., Steidel, C. C., Pettini, M. & Bogosavljević, M. Spectroscopic measurements of the far-ultraviolet dust attenuation curve at z~3. *Astrophys. J.* **828**, 107 (2016).

66. Bergvall, N. et al. First detection of Lyman continuum escape from a local starburst galaxy. I. Observations of the luminous blue compact galaxy Haro 11 with the Far Ultraviolet Spectroscopic Explorer (FUSE). *Astron. Astrophys.* **448**, 513–524 (2006).

67. Inoue, A. K. Rest-frame ultraviolet-to-optical spectral characteristics of extremely metal-poor and metal-free galaxies. *Mon. Not. R. Astron. Soc.* **415**, 2920–2931 (2011).

68. Fisher, D. B. et al. The rarity of dust in metal-poor galaxies. *Nature* **505**, 186–189 (2014).

Acknowledgements

Author contributions

K.S. led the project, and the writing of the manuscript; reduction of the the UVIT data (pipeline, photometry, astrometry) and analysis, SED modelling, dust extinction and escape fraction calculation. S.N.T. contributed to the UVIT data reduction pipeline and interpretation of the photometry. C.S., A.V. and D.S. performed the BPASS modelling as well as interpretation of the result in terms of IGM distribution. A.V. and D.S. wrote the contamination hypothesis part. A.P. performed the spectral fitting of the grism data and

emission-line mapping, BPT diagram. A.B. contributed to the FUV image analysis, noise estimation. A.K.I. performed Monte Carlo simulations of the IGM at the FUV band and at the redshift of the object. M.R., B.E., F.C. and D.E. participated actively in the scientific discussion, interpretation throughout the project and contributed to the final version of the manuscript. M.P. contributed in the MUSE analayis.

Competing interests
The authors declare no competing interests.

Additional information
Extended data is available for this paper at https://doi.org/10.1038/s41550-020-1173-5.

Correspondence and requests for materials should be addressed to K.S.

Reprints and permissions information is available at www.nature.com/reprints.

Publisher's note Springer Nature remains neutral with regard to jurisdictional claims in published maps and institutional affiliations.
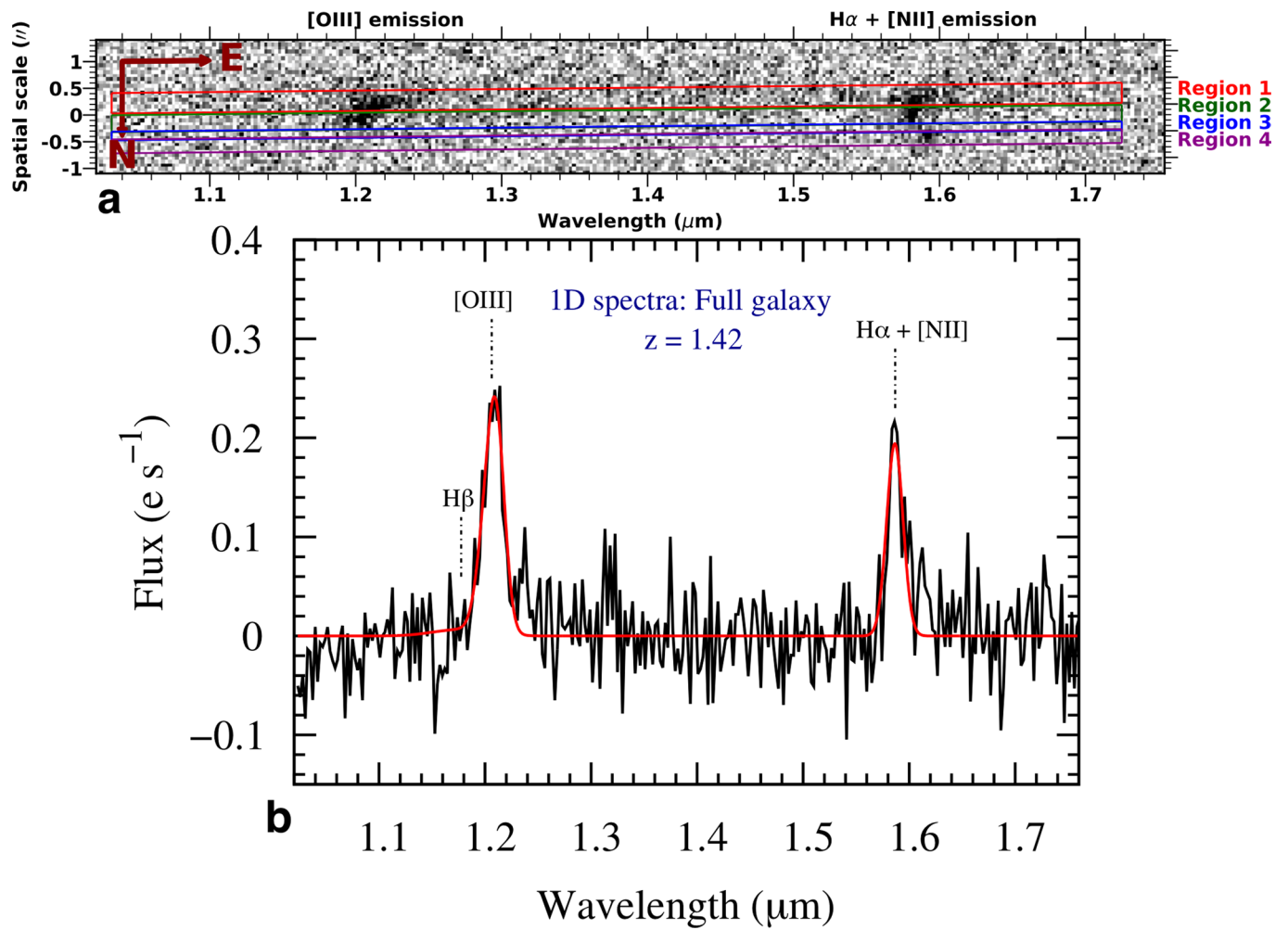
Extended Data Fig. 1 | HST grism (G141) image. a, Coloured rectangular regions (1,2,3,4) marked on the grism image are used to extract spectra for the clumps. North-East directions are marked on the grism image. **b**, 1D spectrum for the full galaxy. Red solid line represents the fitting of the spectrum. Redshift measurement is based on the fitting of Hα+[N II] line alone.
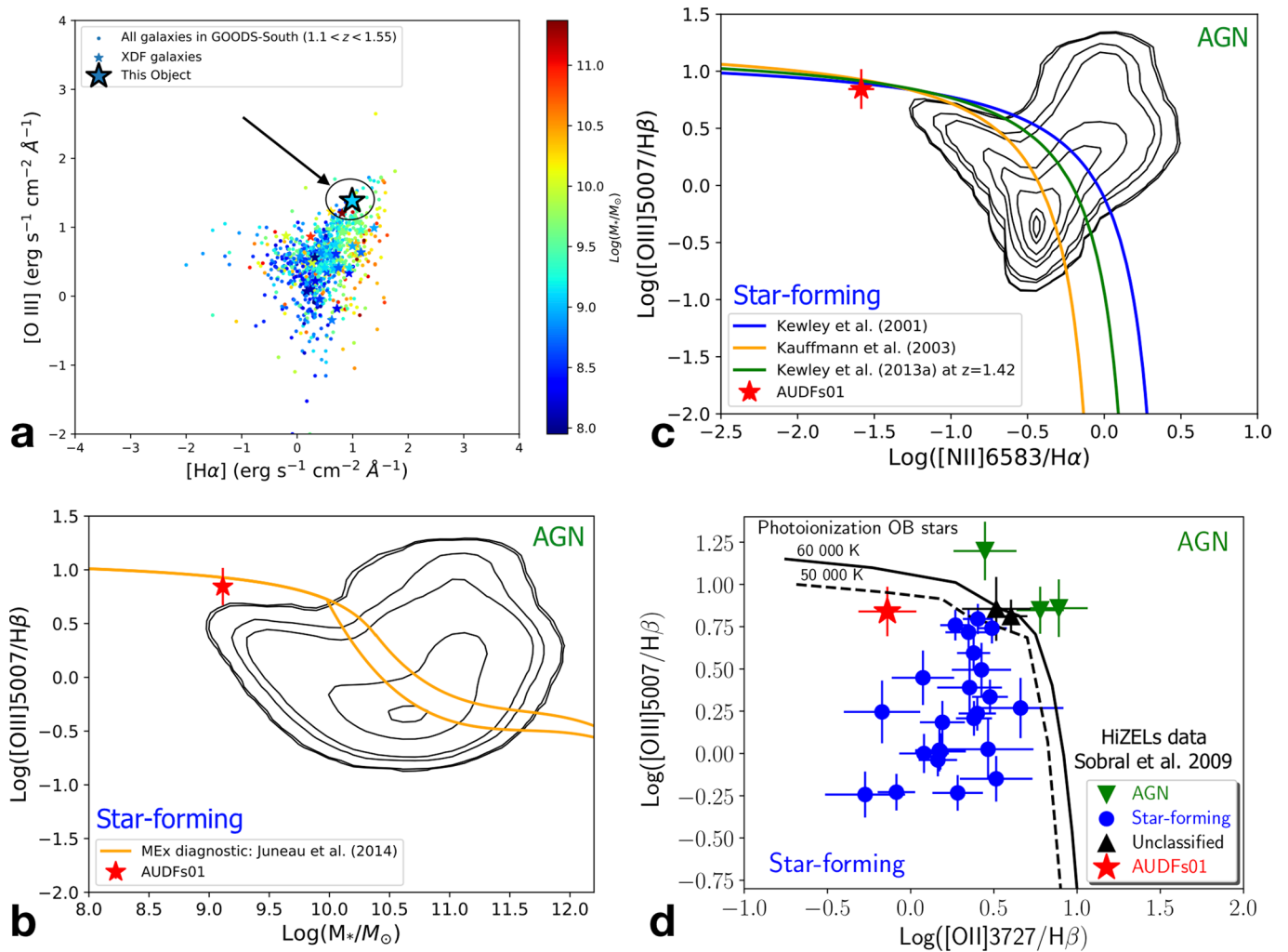
Extended Data Fig. 2 | SF-AGN diagnostic diagram. a, location of the clumpy galaxy AUDFs01 on the Hα - [O III] plane. The line fluxes are measured from HST grism G141 data[20]. AUDFs01 being the only galaxy having highest [O III] flux in the XDF region; the color bar indicates the stellar masses of the galaxies. **b**, **c**, Mass Excitation and BPT diagram using the SDSS galaxies. **d**, location of AUDFs01 on the Sobral et al. (2009) plot. The line ratios for all galaxies except AUDFs01 are taken from z-COSMOS survey[57] at z ~ 0.84. The error bars represent 1σ uncertainties on the flux measurements.
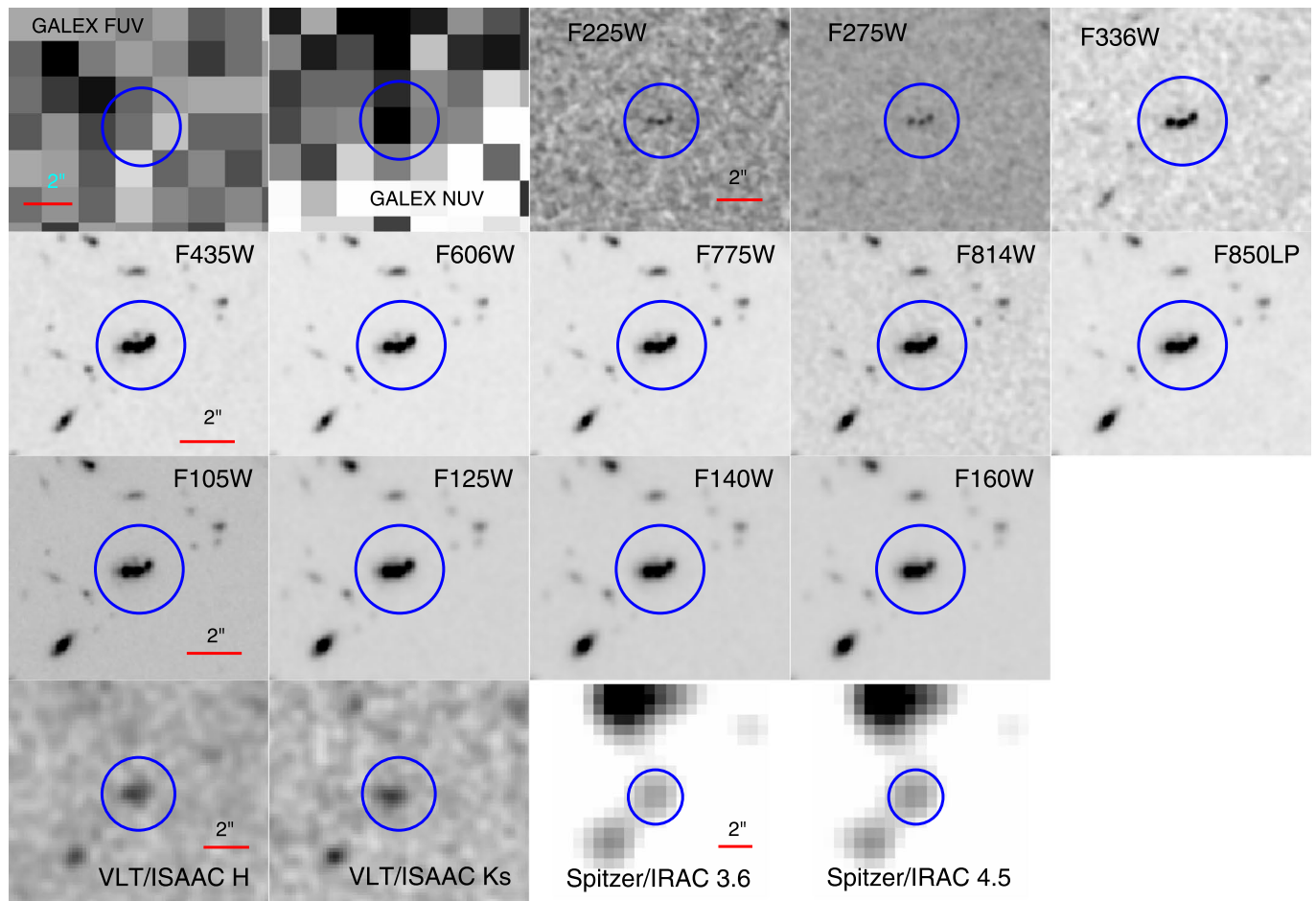
Extended Data Fig. 3 | Postage stamp images. GALEX (FUV, NUV), HST (UV, Optical, IR), VLT/ISAAC (H, Ks), Spitzer/IRAC (3.4, 4.5 micron)-bands. The radius of the blue circle in each panel is 1.6".
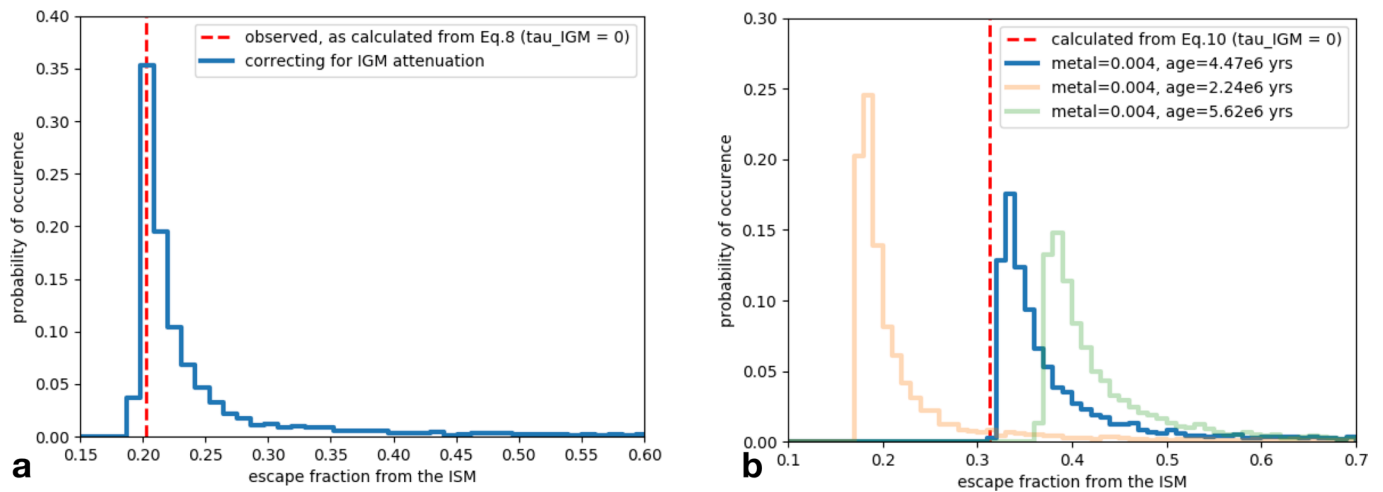
Extended Data Fig. 4 | Distributions of LyC escape fractions. a, For the first method, calculating the LyC escape fraction from the Hα luminosity following Eq. (8). **b**, Following Eq. (10), for the best-fit BPASS model with metallicity $Z = 0.004$, and an age of the stellar burst of ~ 4.5×10^6 years. Other BPASS models, varying ages, are shown with faded lines for comparison. On both panels, the vertical dashed line shows the value of the escape fraction assuming a transparent IGM (following Eq. (8) and Eq. (10)).

Line	flux EW method ($\times 10^{-17}$ cgs unit)	flux1$_{corr}$ (Balmer decrement) ($\times 10^{-17}$ cgs unit)	flux2$_{corr}$ (UV β) ($\times 10^{-17}$ cgs unit)	L$_\beta$ ($\times 10^{41}$ erg s^{-1})
O II 3726.0	0.48 ± 0.009	6.64 ± 0.12	2.44 ± 0.045	3.04 ± 0.06
O II 3729.0	0.69 ± 0.012	9.52 ± 0.16	3.50 ± 0.06	4.36 ± 0.07
Hβ 4861.0	1.86 ± 0.78	14.63 ± 6.1	$6.7(\mathbf{8.2}) \pm 2.7$	8.30 ± 3.4
O III 4959.0	5.53 ± 0.40	41.7 ± 3.0	19.3 ± 1.4	24.0 ± 1.7
O III 5007.0	16.59 ± 1.20	122.5 ± 8.8	57.2 ± 4.1	71.2 ± 5.1
N II 6548	0.08 ± 0.007	0.36 ± 0.03	0.20 ± 0.02	0.25 ± 0.02
Hα 6563.0	9.33 ± 0.96	41.3 ± 4.2	23.46 ± 2.4	29.2 ± 3.0
N II 6583	0.24 ± 0.022	1.06 ± 0.09	0.60 ± 0.05	0.75 ± 0.07

Extended Data Fig. 5 | Emission-line fluxes and luminosities. Col2: line flux as measured in the HST grism G141; [O II] is from MUSE catalogue. col3: line fluxes after foreground dust plus internal extinction correction using Balmer decrement. Col4: same as col3 but internal extinction (E(B-V)=0.13) due to UV beta slope; the value of Hβ (marked bold-face in the bracket) is what would be expected as per the internal Balmer decrement given the measured Hα. Col5: line luminosity following UV beta slope.

CIGALE Module	physical parameters	parameter range (best fit - bold face)
Sfh2exp	τ_{main} (Myr)	**50**, 100, 200, 400, 700, 1000, 2000, 4000
	τ_{burst} (Myr)	50, **100.**, 150.
	f_{burst}	0.01, 0.02, 0.04, **0.06**, 0.08, 1.0
	Age_{main} (Myr)	20., 50., **100**, 200, 300, 500, 600, 700, 1000, 2000, 4000
	Age_{burst} (Myr)	**2.0**, 3.0, 4.0, 5.0, 10.0
BC03	IMF	0 (**Salpeter**), 1 (Chabrier)
	Metallicity	0.0004, **0.004**, 0.008, 0.02
Nebular	Ionization parmeter (logU)	-3.0
	fraction of LyC photons escape f_{esc}	0.0, 0.1, 0.2, 0.3, 0.4, **0.5**, 0.6, 0.65, 0.7, 0.75, 0.8
	fraction of LyC photons absorbed f_{dust}	0.0, 0.05, 0.1, **0.15**, 0.2
	Line-width (km/s)	300.0
Dustatt-Calzetti	E(B-V)$_{young}$ (mag)	0.11, 0.12, 0.13, **0.15**, 0.17, 0.19, 0.2, 0.22
	E(B-V)-factor	**0.44**, 0.6, 0.9, 1.0
	uv-bump-wavelength (nm)	217.5
	uv-bump-width (nm)	35.0
	uv-bump-amplitude	1.0
	(δ) modifying the attenuation curve	-0.5
dl2014	α (as in $dU/dM \propto U^\alpha$)	2.0
restframe-parameters	beta-calz94	True
	Dn4000	True
	IRX	True
	EW_{lines} (nm)	372.7/1.0, 486.1/1., 500.7/1. 656.3/1., 658.3/1.
	Luminosity	F154W, N242W, V$_{B90}$
	Color	FUV-NUV, NUV-r$'$

BPASS Parameter	**Allowed values**
Age [yrs]	5×10^6, 10^7, 5×10^7, 10^8, 5×10^8
Metallicity [Z]	10^{-5}, 10^{-4}, 0.002, 0.004, 0.008, 0.020, 0.040
Column density [N_H cm^{-2}]	10^{16}, 10^{17}, 10^{18}
Model	single, binary

Extended Data Fig. 6 | SED fitting parameters for CIGALE and BPASS. The best-fit parameters for cigale modelling are indicated by the bold-face letters. Dn4000 represents the ratio of the average flux density in two two narrow bands, $3850 - 3950$ Å and $4000 - 4100$ Å. IRX refers to the infrared excess.

Filters	Full galaxy AB mag	C1 AB mag	C2 AB mag	C3 AB mag	C4 AB mag
F154W	25.84 ± 0.34				
N242W	25.60 ± 0.10				
F225W	25.45 ± 0.13				
F275W	24.73 ± 0.12	26.74 ± 0.04	26.76 ± 0.049	26.88 ± 0.05	28.94 ± 0.23
F336W	24.19 ± 0.05	26.25 ± 0.042	26.16 ± 0.049	26.47 ± 0.05	28.75 ± 0.23
F435W	24.21 ± 0.07	26.18 ± 0.032	25.96 ± 0.032	26.41 ± 0.023	28.85 ± 0.09
F606W	24.20 ± 0.10	26.12 ± 0.038	25.76 ± 0.039	26.35 ± 0.032	28.94 ± 0.087
F775W	24.16 ± 0.05	26.09 ± 0.045	25.72 ± 0.042	26.38 ± 0.023	29.04 ± 0.11
F814W	24.14 ± 0.20	26.04 ± 0.055	25.68 ± 0.049	26.33 ± 0.044	29.00 ± 0.26
F850LP	23.77 ± 0.04	25.86 ± 0.05	25.59 ± 0.047	26.22 ± 0.038	28.88 ± 0.16
F105W	23.61 ± 0.21	25.49 ± 0.29	25.40 ± 0.25	25.93 ± 0.25	28.56 ± 0.51
F125W	23.40 ± 0.30	25.46 ± 0.36	25.34 ± 0.22	25.91 ± 0.21	28.56 ± 0.70
F140W	23.41 ± 0.36	25.46 ± 0.36	25.28 ± 0.23	25.89 ± 0.22	28.58 ± 0.74
F160W	23.42 ± 0.20	25.47 ± 0.36	25.24 ± 0.22	25.88 ± 0.22	28.61 ± 0.74
VLT/ISAAC H	23.74 ± 0.37				
VLT/ISAAC Ks	23.95 ± 0.26				
Spitzer $3.5\mu m$	23.53 ± 0.13				
Spitzer $4.5\mu m$	23.29 ± 0.14				

Extended Data Fig. 7 | Magnitudes of the galaxy AUDFs01 and its clumps. Magnitudes of the galaxy AUDFs01 and its clumps at different passband. All magnitudes are aperture and foreground dust corrected.